INT. REVIEWS IN PHYSICAL CHEMISTRY, 2004
VOL. 23, NO. 3, 375–433

Taylor & Francis
Taylor & Francis Group

Solid water clusters in the size range of tens–thousands of H_2O: a combined computational/spectroscopic outlook

VICTORIA BUCH*
The Fritz Haber Institute for Molecular Dynamics,
The Hebrew University, Jerusalem, 91904, Israel

SIGURD BAUERECKER
Institut für Physikalische und Theoretische Chemie,
Technische Universität Braunschweig, D-38106 Braunschweig
and
Institut für Küstenforschung, GKSS-Forschungszentrum GmbH,
D-21502 Geesthacht

J. PAUL DEVLIN
Department of Chemistry, Oklahoma State University, Stillwater, OK 74078

UDO BUCK
Max-Planck-Institut für Strömungsforschung, D-37073 Göttingen, Germany

JAN K. KAZIMIRSKI
Industrial Chemistry Research Institute, 8 Rydygiera Street,
01-793, Warsaw, Poland

A joint computational and experimental effort was directed towards the understanding of large solid water clusters. The computations included structure optimizations and calculations of OH stretch spectra for select sizes in the range $n = 20$–931. The measurements focused predominantly on OH stretch spectroscopy as a function of mean cluster size. FTIR spectra are discussed for the size range of tens to hundreds-of-thousands of molecules. Photofragment spectroscopy in molecular beams is shown to be a sensitive probe of the outer cluster surfaces. The crucial element of the different experimental approaches is the control and the estimation of the mean cluster sizes. The combined experimental and computational results are consistent with the physical picture of quasi-spherical nanocrystals with disordered reconstructed surface layers. The surface reconstruction can be viewed as the outcome of recombination of surface dangling atoms, to increase the number of hydrogen bonds. The hydrogen bonds within the mostly crystalline subsurface layer are stretched by the interaction with the disordered component. The emergence of the (strained) crystal core occurs at a size of a few hundred H_2O. Smaller clusters are described as compact-amorphous.

* Corresponding author. viki@fh.huji.ac.il

International Reviews in Physical Chemistry ISSN 0144–235X print/ISSN 1366–591X online
http://www.tandf.co.uk/journals
DOI: 10.1080/01442350412331316124

Contents PAGE

1. Introduction

During the last few years, study of gaseous water clusters has become an important branch of H_2O research. This is since (a) detailed spectroscopic data became available for $(H_2O)_n$ in a broad size range, (b) a combination of theoretical and experimental investigations on water clusters are a valuable source of information on interactions between water molecules (this information can be further used for study of 'real life' condensed phases), (c) clusters can be considered a bridge between the gas phase and the condensed phases, and therefore evolution towards condensed phase structure and dynamics as a function of size is of interest, (d) H_2O particles and perhaps also clusters play an important role in atmospheric and space chemistry [1–4], (e) water clusters display a variety of interesting behaviours, and are therefore worthy of basic science research for their own sake.

This study presents our joint efforts to advance the understanding of cold solid $(H_2O)_n$ clusters in the size range of tens–thousands of molecules. Experimental studies focus predominantly on infrared OH-stretch spectroscopy of the clusters; this vibrational mode is known to be an excellent probe of hydrogen bonding. Several approaches are described for addressing the challenge of controlling the mean size of the clusters. The interpretation is carried out with the help of calculations of low energy structures and spectra for representative cluster sizes ($n = 20$–22, 48, 123, 293, 600 and 931). Perhaps the most interesting feature of this size range is the onset of crystallinity in $(H_2O)_n$, at a size of a few hundred molecules.

1.1. *General structural characteristics*

Representative low energy cluster structures, which will be discussed in more detail below, are shown in figures 1 and 2. Water cluster structure can be characterized in two stages. First, the O-structure is defined. The skeleton of the oxygen atoms determines the shape of the cluster, the number of hydrogen bonds, and the hydrogen-bond coordination of individual molecules. Another cluster feature is the H-structure, i.e., the position of the H-atoms within the network of the hydrogen bonds.

Each O-structure is associated with numerous distinct potential minima, corresponding to different H-structures. This multiplicity of H-structures originates from the fact that an H-atom may adopt one of two possible positions on a near-neighbour O···O axis (i.e., it may be chemically bonded to either of the two O-atoms, and hydrogen-bonded to the other). The number of unrestricted configurations would be then 2^K, where K is the number of hydrogen bonds. The allowed configuration space is however restricted by the constraint that each O is chemically bonded to exactly two H-atoms. Even within this constraint, a multitude of possible H- (or orientational) arrangements is possible. This multitude is a cluster analogue of the well-known orientational disorder (or 'proton disorder') characteristic of the crystalline ice Ih, and of the closely related ice Ic. (Ice Ih is the common thermodynamically stable form at low pressures; ice Ic was observed in low temperature vapour deposits and in nanocrystals [5–10].) It has been realized for a long time that different orientational arrangements of ice are nearly isoenergetic [11–13]. However in clusters, energies of different H-structures corresponding to the same O-frame may differ significantly; this fact has been discussed in detail by Singer *et al.* [14, 15]. The broad energy range is largely a surface effect; specifically, the presence of neighbouring dangling-H atoms raises the cluster energy substantially due to electrostatic repulsion.

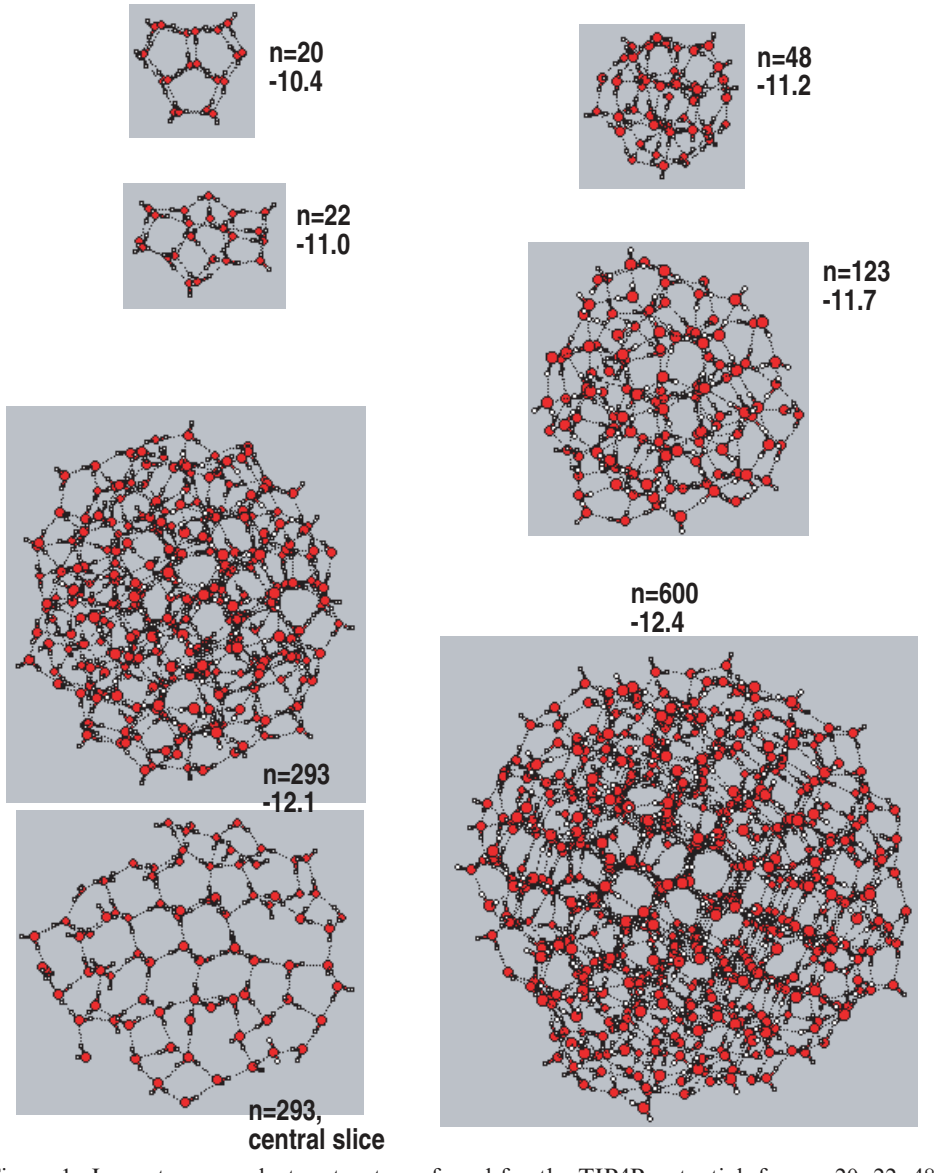

Figure 1. Lowest energy cluster structures found for the TIP4P potential, for $n = 20$, 22, 48, 123, 293 and 600. Minimum energies in kcal/(mol H_2O); zero of energy corresponds to non-interacting molecules. For $n = 239$, bottom figure shows a central slice; note incipient crystallinity in the form of six-membered rings at the centre.

We now consider the onset of crystallinity. Crystal structure is dictated by the stability of a three-dimensional periodic molecular arrangement; therefore, a minimum amount of molecular material is needed to obtain crystalline particles. This amount varies considerably for different atomic and molecular systems; it depends on the viability of the crystal arrangement at the surface, and on the characteristics of the intermolecular bonding. For example, for CO_2 nanoparticles, bulk crystal structure appears favourable both for the surface and for the interior, and the onset of crystallinity occurs already for a few tens of molecules [5, 6, 16–18]. On the other

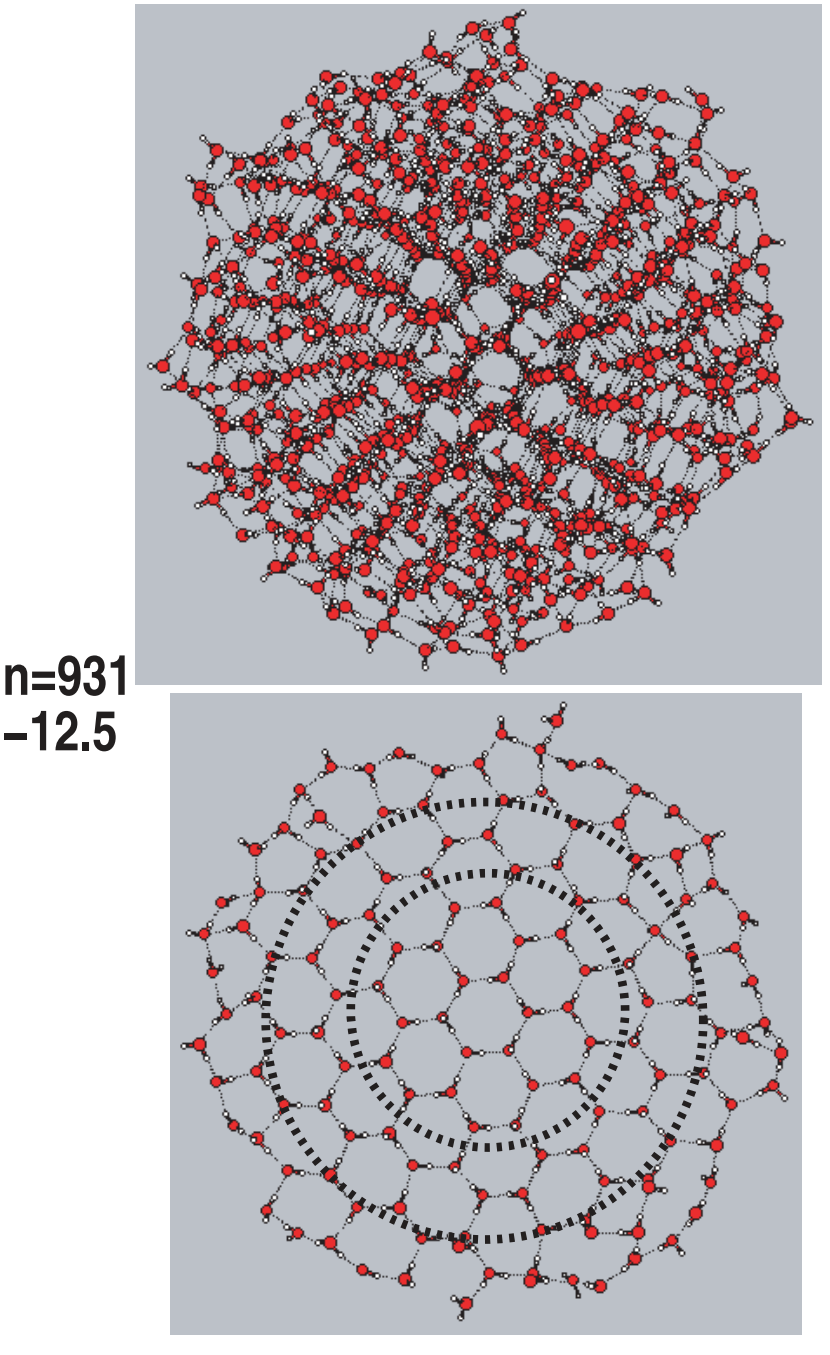

Figure 2. Lowest energy cluster structures found for the TIP4P potential for $n = 931$. Minimum energy in kcal/(mol H_2O); zero of energy corresponds to non-interacting molecules. For comparison, the minimum TIP4P energy calculated for ice Ic and ice Ih is -13.64 and -13.65 kcal/(mol H_2O), respectively [13]. Bottom figure shows central bilayer slice; note crystallinity in the middle, and surface disorder. The circles denote boundaries between crystal interior, subsurface and surface, obtained from best fit to experimental spectra.

hand, for Ar clusters, the transition to the bulk crystal structure does not seem to take place up to $\sim 10^5$ atoms [19]. It has been shown in past electron diffraction studies by Torchet *et al*. [5, 6], that in ice clusters the onset of crystallinity occurs somewhere between $n \sim 200$ and $n \sim 1000$.

Based on subsequent spectroscopic and computational studies, Devlin, Buch *et al*. suggested the following physical picture for ice nanoparticles [21–23]. Water ice Ih and ice Ic correspond to nearly perfect three-dimensional tetrahedral hydrogen-bond networks [11, 12]; the O-arrangement is periodic, while (as noted above) molecular orientations are random within the constraint of completeness of the network. This structure is favourable for the interior but not necessarily for the surface. If a cluster is cut out of a crystal structure, numerous 'dangling' H- and O-atoms, with unsatisfied hydrogen bond coordinations, appear at the surface. However the dangling atoms can recombine to form additional, albeit strained, hydrogen bonds, at the expense of tetrahedral symmetry and crystal periodicity [18, 20–23]. Thus the low energy ice nanocrystal structures correspond to approximately spherical nanoparticles with crystal interior, and a disordered 'reconstructed' (recombined) surface; this arrangement constitutes a compromise between a tendency to increase the *number* of hydrogen bonds, and the tendency to optimize their *geometry*. Moreover formation of a crystal-like tetrahedral bond network requires a water cluster size with a sufficient amount of 4-coordinated 'interior'; and therefore below the size of a few hundred molecules low energy cluster structures are amorphous.

1.2. *General characteristics of cluster OH stretch spectra*

The computed and measured infrared spectra, to be discussed in detail in the following sections, are shown in figures 3–6. Computations of the OH-stretch absorption bands for cluster sizes in the range $n = 20$–931 (figure 3) will be used to interpret FTIR spectra measured as a function of the mean cluster size (figures 4 and 5). The FTIR spectra, measured in two different laboratories cover the range $\langle n \rangle \sim 20$–$400$ (figure 5) and $\langle n \rangle \sim 300$–$30{,}000$ (figure 4); the bottom two spectra of figure 4 are comparable to the top one in figure 5. The spectra shown in figure 6 were obtained in molecular beams, using photofragment detection. The latter technique probes predominantly infrared absorption by undercoordinated molecules of the cluster surface; the corresponding lineshape, which is quite different from FTIR, is interpreted with the help of calculations of the cluster *outer surface spectra*.

The main value of the OH-stretch spectrum is its high sensitivity to the OH-stretch frequency. In the smallest clusters considered, with a few tens of molecules, about half of H_2O are 3-coordinated, with either dangling-H (d-H) atoms, or dangling-O (d-O). A d-H atom is unbonded; a d-O atom has a single hydrogen bond. Molecules with a d-H give rise to a weak but sharp and well-separated *free*-OH band at $\sim 3700\ cm^{-1}$; this band was shown in the past to be an interesting probe of the cluster surface area, and of surface interactions with adsorbates [22]. The lower-frequency *bonded*-OH band is characterized by large intensity, and large width of several hundred cm^{-1}. As shown in past investigations and discussed in detail in the following sections, the undercoordinated molecules absorb at both ends of the bonded-OH band (see figure 7, and [22, 24]). The result is a broad absorption spectrum for small cluster sizes. The 4-coordinated contribution at the centre of the band becomes dominant as the cluster size increases. The spectrum becomes peaked; moreover the peak frequency shifts to the red, approaching ice values, as particles

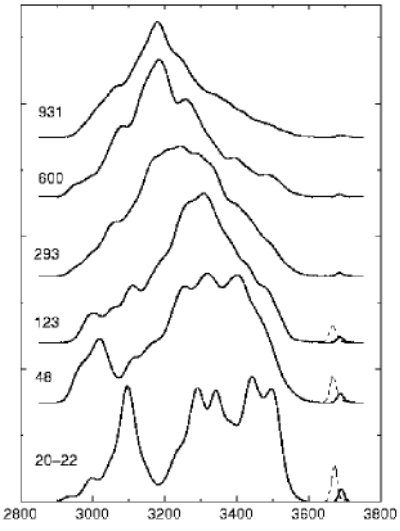

Figure 3. Calculated spectra of $(H_2O)_n$ clusters. For $n = 20$–22, the spectrum was averaged over 10 lowest lying configurations which were found in TIP4P, and over three cluster sizes. For $n = 48$, 123, and 293, the spectrum was averaged over 10 lowest energy configurations found for each size. For $n = 600$ and 931, the spectrum corresponds to a single lowest energy configuration found. For $n = 20$–123, the dot-dashed line corresponds to the free-OH band redshifted by $20\,cm^{-1}$ and amplified by factor 3, to represent roughly the effect of N_2 adsorbate.

develop well-crystallized cores with increasing size. The spectrum of the outer, largely undercoordinated, cluster surface layer (which is probed by the vibrational predissociation technique discussed in Section 5 [24–26]) does *not* narrow down significantly with increasing cluster size, as seen in figure 6.

One should emphasize at this point that the widths and the lineshapes of the $(H_2O)_n$ infrared spectra are determined by the *interplay* between the bond strength distribution, and the dynamic coupling between vibrations of different OH bonds. (As discussed in the next section, the substantial intermolecular coupling can be modelled as a dipole–dipole interaction. Intramolecular coupling in condensed phases is significantly smaller than in gaseous H_2O [106].) In the limiting case of crystal ice, the $\sim 300\,cm^{-1}$ width of the spectrum is due overwhelmingly to the coupling, since all the H-bonds are nearly equivalent [27]. The ice spectrum is well approximated by the top spectrum of figure 4, corresponding to a 12 nm nanocrystal. The influence of the intra- and intermolecular coupling on the OH lineshapes can be minimized by studying particles with HDO isotopically isolated in D_2O, rather than pure $(H_2O)_n$; the corresponding OH-stretch spectra were in fact shown to be significantly narrower [21, 125]. As the cluster size decreases, the spectrum is increasingly affected by the broad distribution of hydrogen bond strengths, but the effect of the coupling is still significant; see figure 7.

The modification of the spectra by intermolecular coupling is commonly (and often incorrectly) ignored in the literature addressing OH spectroscopy of H_2O-containing systems, by a variety of techniques. The coupling not only contributes significantly to the width, but also results in *collective* vibrational excitations. Peaks observed in the measured spectra may be due to select collective vibrations, with phase relations favoured by a given experimental technique, rather than to a large

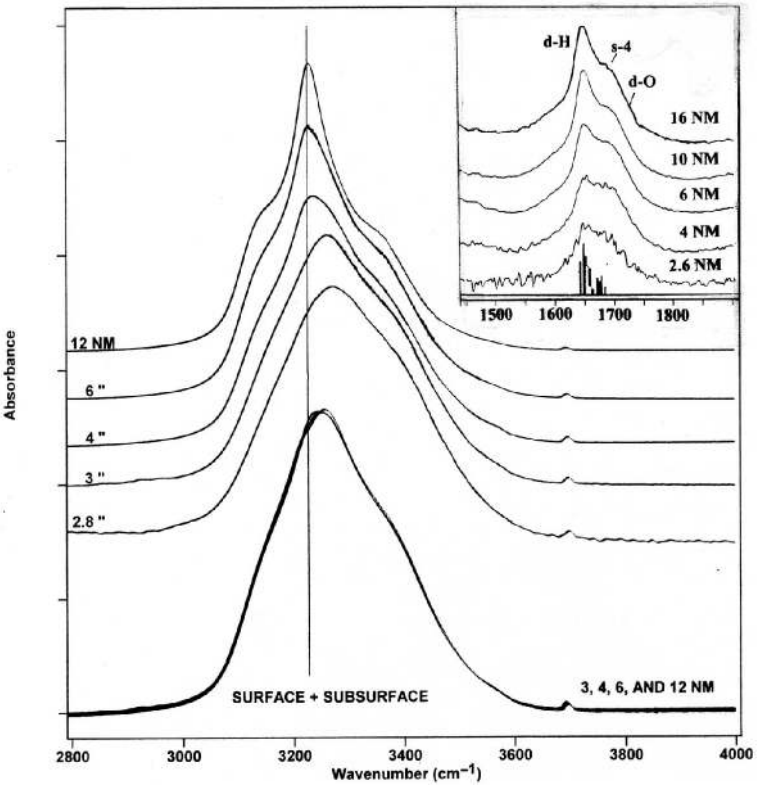

Figure 4. Dependence of the O–H stretch band complex on particle size ranging from dominantly crystalline core (12 nm), through crystalline but with no core component (3 nm) to largely amorphous particles (2.8 nm). The corresponding average numbers of molecules per cluster, from top to bottom, are about 27,000 (12 nm), 3400 (6 nm), 1000 (4 nm), 400 (3 nm), and 340 (2.8 nm). The four bottom overlayed spectra show that removal of the crystalline-core component for particles larger than 3 nm yields the same combined surface and subsurface spectra of the 3 nm particles. The inset shows the surface water molecule bending-mode spectra versus particle size. The bottom histogram represents a distribution of bending-mode oscillator strength versus frequency obtained from *ab initio* calculations for a range of local ice configurations. The labelled assignments are based on those calculations. The notation s-4 pertains to 4-coordinated surface molecules with a coordination shell typically distorted from tetrahedrality. The d-H band pertains to 3-coordinated d-H molecule.

density of OH oscillators at a given frequency [27]. For example, the prominent central peak in the ice nanocrystal spectrum (figure 4, top) was shown to be due to a collective in-phase asymmetric stretch excitation, corresponding to a large transition dipole [27, 28].

1.3. *Past investigations of water clusters: a brief overview*

For the water dimer, a sequence of past experimental and theoretical studies (see, e.g., [29, 30]) demonstrated conclusively a near-linear hydrogen-bonded global minimum in the potential energy surface (PES). $(H_2O)_n$, $n \geq 3$ clusters have been investigated extensively for a long time, in theoretical studies employing electronic structure techniques (e.g., [31–58]), a variety of analytical potentials (e.g., [14, 15, 59–86]), and a combination of both (e.g., [87–97]). For $n = 3$–5, a cyclic lowest energy

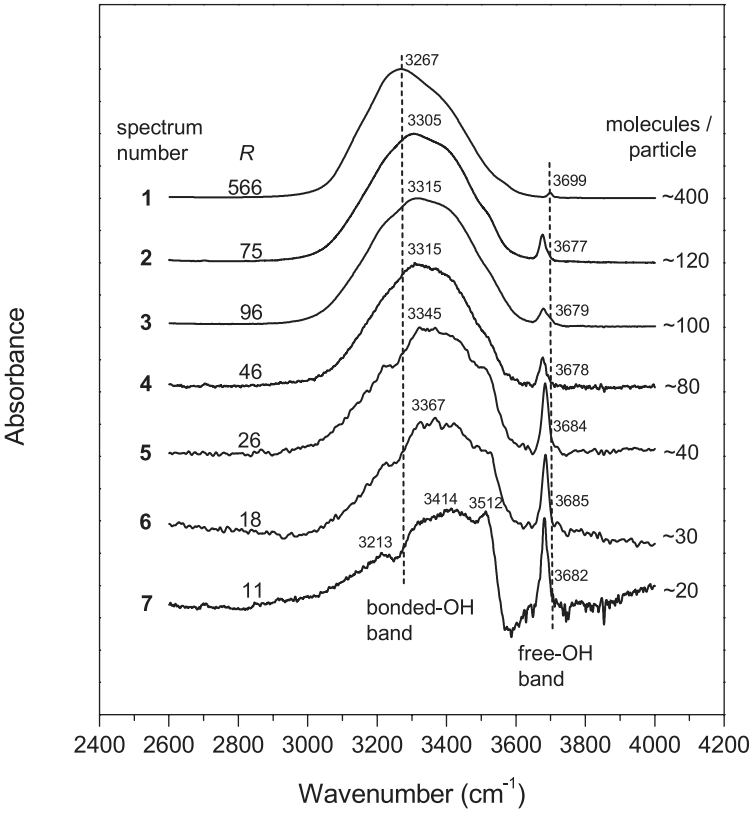

Figure 5. Dependence of the O–H stretch band complex on particle size ranging from $n \sim 400$ to low tens; estimated average size is marked on the figure as molecules per particle (last column). Peak positions are indicated in cm^{-1}. *R* marks the ratio of the integrated absorbance of bonded-OH band to free-OH band (second column). The trend of blueshift of the bonded-OH band with decreasing particle size as seen in figure 4 is continued in accordance with the computed spectra (figure 3). The spectral features due to companion bonded-OH of d-H molecules at 3200 cm^{-1} and bonded-OH of d-O molecules at 3500 cm^{-1} become increasingly pronounced in spectra 5–7. The free-OH band at 3700 cm^{-1} is redshifted by about 20 cm^{-1} and increased in its intensity by a few hundred percent as a result of N_2 adsorbate on the clusters of spectra 2–7.

structure has been predicted, with the basic structural unit of a single proton donor–single acceptor water molecule. At $n = 6$, a number of nearly isoenergetic two- and three-dimensional low energy isomers were predicted; the exact energy ordering has been a subject of considerable discussion (see, e.g., [38, 55, 87–89, 96]). For the octamer, two very stable cubic structures (S_4 and D_{2d}) were predicted theoretically [66, 67, 87, 91]. A series of far-infrared vibration-rotation-tunnelling (VRT) [98] (and references therein) and infrared laser spectroscopic studies [99] confirmed a cyclic structure for $n = 3$–5. For $n = 6$, the isomers observed experimentally until today include a cage (VRT study [100]), a ring (infrared spectrum in He droplets [101]), and a book (size-selected vibrational spectroscopy [102, 103]). The measured size-selected infrared spectra of $(H_2O)_n$ in the $n = 7$–10 range were assigned to single cage structures [104–107]; the structures can be viewed as derived from the octamer cube, by subtraction or addition of molecules. Similar conclusions were drawn from

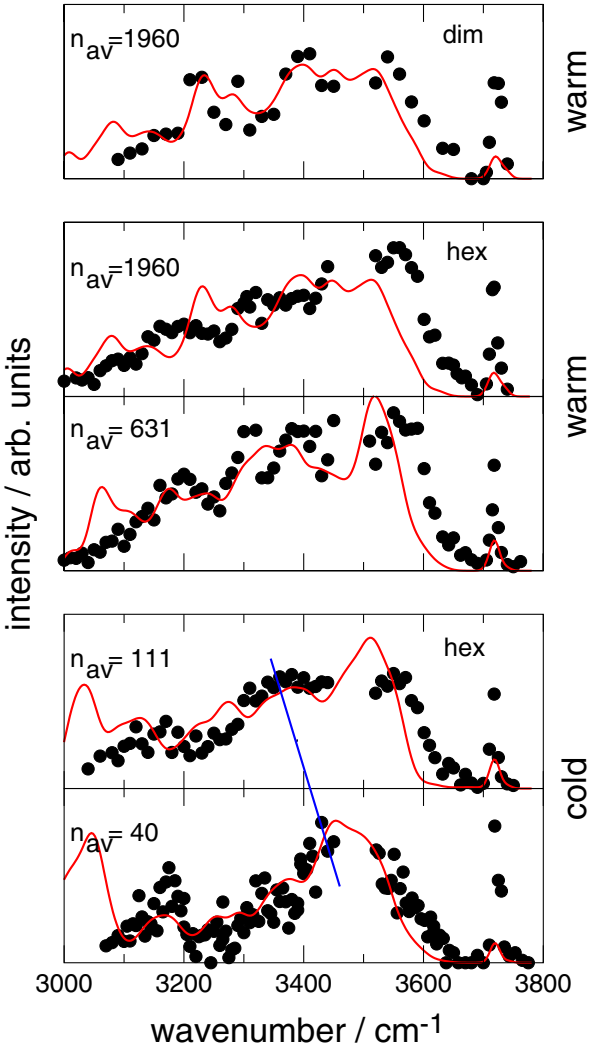

Figure 6. Measured OH stretch photofragment spectra (full points) detected at $(H_2O)_4H^+$ (hexamer parent) and $(H_2O)H^+$ (dimer parent, top panel only) for the average cluster sizes indicated. The continuous lines are calculated surface spectra for $n = 48$, 123, 600, and 931; averaging as in figure 3. The straight line in the bottom two panels indicates the shift of intensity peaks for small clusters which is caused by the decreasing number of amorphous 4-coordinated surface molecules.

the double resonance ion-dip infrared experiments on water clusters connected to benzene [38, 108, 109], and to phenol [110, 111]. In particular, the stable symmetric cube structures of the octamer were reported for the $(H_2O)_8$-benzene cluster [112], and for water clusters with the phenol chromophore [113].

For the size range $n = 11$ to ~ 30, considerable insight has been gained from theoretical studies (see, e.g., [14, 15, 45, 54, 64, 69, 75, 77, 81, 82, 84, 85, 92, 93]). The global minima in this range can be viewed as 'multiple fused cage' structures. Most recently, structural evolution as a function of size in this range was addressed systematically by Hartke [85], with the TIP4P [114] and TTM2-F [115] potentials.

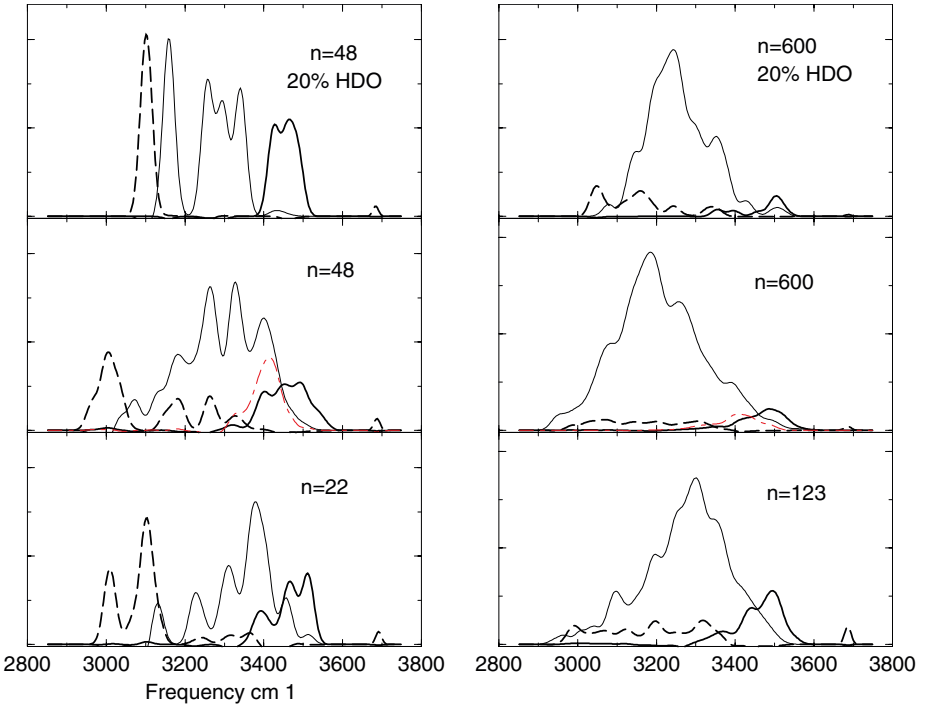

Figure 7. Contributions to cluster absorption spectra from different hydrogen-bond coordinations. Spectra were calculated for lowest energy configurations found in TIP4P for each size. Thin solid line – 4-coordinated molecules; thick solid line – 3-coordinated d-O molecules; dashed line – 3-coordinated molecules with a d-H. (The contributions of other coordinations, two and five, are small.) The two top spectra pertain to isotopically mixed clusters 20% HDO, 80% D_2O; the rest pertains to $(H_2O)_n$. The dot-dashed curves in the middle panels show contributions to 4-coordinated spectra from molecules donating protons to 3-coordinated d-H molecules.

Clusters at the low end of this size range have been described by him as 'all surface'. Increase in size is marked by the appearance of three-dimensional 'centred cage' forms with one or two 4-coordinated core molecules in the interior. A number of theoretical studies focused on simulations of the melting transition in water clusters (see, e.g., [59–61, 83]), and on investigations of 'special' structures which were proposed to be particularly interesting and/or stable. The proposed special forms included clusters composed of cubic octamer-like subunits [65], tubes of four-, five- and six-membered water rings [56, 66, 67, 86], flat sandwich-like structures [80], and large spheroid single cages [14, 15, 47, 57, 58]. Recently, an intriguing suggestion was made of icosahedral cluster structures; these structures are derived from a crystal made of alternating hexamer sheets in boat (as in ice Ih) and chair (ice Ic) configurations [116].

Starting from sizes of 'several tens of molecules' *investigation of the evolution of general structural characteristics as a function of mean size* appears more meaningful than the search for a single ground state for consecutive cluster sizes, for any potential. This is since very numerous low energy structures of similar energies are expected for each size. Determination of the exact energy ordering of these structures

would require potentials of presently unavailable accuracy. Moreover most of the available experimental data for neutral $(H_2O)_n$ clusters pertain to *distributions* of cluster sizes, rather than to a single known size [5–10, 21, 22, 24, 117–122], although advances have been made in spectroscopy of size-selected water clusters doped with a Na atom [24].

Experimentally, there have been two distinct approaches to the preparation of cold water particles in the range of hundreds to many thousands of molecules, for studies of basic physical-chemical properties. Samples of ice nanoparticles have been prepared using expansion beams [5–10, 24, 118, 119, 122], and by collisional cooling in cluster cells [21, 22, 117, 120, 121, 123]. While typical experimental set-ups allow for manipulation of the cluster size distribution, determination of the resulting sizes is a non-trivial problem. Knowledge of ice particle size is essential to obtain full value from structural and spectroscopic measurements. The average size of ice particles in the expansion beams has been estimated from the breadth of electron diffraction peaks [5–10], and by doping the particles with sodium atoms to permit detection by single photoionization [24, 26] (see Section 5). For particles of average diameter >15 nm, in arrays prepared using collisional cooling methods, sizes have been approximated using transmission electron microscopy [120, 121]. Such size measurements are not readily adaptable to the FTIR studies in cluster cells, discussed in Sections 3 and 4. There, size estimates are carried out by spectroscopic means, i.e., by comparing integrated intensity of the H-bonded OH stretch band (which is proportional to the cluster volume), to the intensity of spectral features that are proportional to the cluster surface area. One such feature is the free-OH band, which originates from the cluster surface [21, 22, 124]. Another approach to estimate the surface area is to cover the nanoparticles by a monolayer of CF_4, and to measure the corresponding adsorbate infrared band intensity [18, 21, 22, 125].

Section 2 describes calculations of cluster structures and spectra, carried out by the Buch group. Section 3 addresses FTIR spectroscopy of ice-nanoparticles in the size range of 200–1,000,000 molecules, by Devlin *et al.*; methods to estimate particle size are described, and size-dependent spectra are presented and analysed. Recently, Bauerecker *et al.* succeeded to extend FTIR measurements of water cluster spectra as a function of mean size, down to particles containing tens of molecules. The pertinent spectra are presented and discussed, for the first time, in Section 4. Section 5 focuses on the spectroscopy of the outer disordered layer of $(H_2O)_n$ clusters, for sizes from tens to thousands of molecules, as probed by a vibrational predissociation method developed by Buck *et al.* [24, 25]. A summary and final comments are presented in Section 6.

2. Calculations of low energy structures and spectra of water clusters

Structure optimization of water clusters has been addressed in the past by a variety of approaches, including basin hopping [54, 75, 76], evolutionary algorithms [72, 81, 84, 85], reaction coordinate analysis [77], graph invariants [126], the pivot method [82], Gaussian density annealing [68], and a diffusion equation scheme [127]. Kazimirski and Buch developed recently a computational scheme, geared specifically to the water cluster problem; the aim was to locate and characterize low energy structures for relatively large sizes ($n=48$, 123, and 293) [23, 128]. The resulting cluster structures, together with additional ones for $n=600$ and 931 obtained by similar methodology are used here to calculate and interpret the experimental spectra.

Before discussing the cluster structures, we should like to emphasize the formidable difficulties and uncertainties associated with this optimization problem. The main difficulty is the 'rugged energy landscape', i.e., a multitude of cluster minima separated by high barriers. Moreover, a collection of water molecules which are brought in contact, bond with each other quite efficiently during simple minimization; and further structure optimization is associated with a relatively small energy gain, percentage-wise. One may note in this context that the latent heat of crystallization of amorphous ice is $\leq 2\%$ of the heat of sublimation [11]. Latent heats of phase transitions between different crystal ice forms are of order of $\sim 1\%$ of the heat of sublimation [11].

Moreover, because of the high dimensionality, one should worry about very incomplete sampling of the configuration space. While our optimization scheme was shown to lower effectively the energy of the particles, the final optimized structures depend on the choice of the input configurations. This result is hardly surprising, considering the huge number of nearly isoenergetic cluster isomers in the pertinent size range. Thus, finding the ultimate lowest energy cluster structure is very difficult and probably irrelevant; rather, our more modest and general goal is location of 'typical' low energy structures. One should still worry to what extent the resulting *qualitative* cluster characteristics depend on the potential, and on the choice of the input configurations. We are encouraged in this respect by reasonable consistency of the computed and experimental results, as discussed below.

2.1. *Overview of the optimization scheme*

The general optimization strategy includes three stages. The first employs classical molecular dynamics (MD). Search for low energy structures by classical trajectories is not a new idea; in fact, simulated annealing (i.e., gradual cooling by MD of an initially warm structure) has been among the first tools applied. The well-known problem is trapping of trajectories in high energy minima. Here, we employ a variant which proved to be surprisingly effective in locating low lying minima. A set of relatively long classical trajectories is run at different energies, corresponding to temperatures in the range 100–200 K. Structures along the trajectories are minimized at constant intervals. At low temperatures, molecular mobility is limited; and only minima in the vicinity of the initial structure are accessed. In the high temperature regime the system is mobile, and probes numerous minima; however high energy structures are preferred. There is some intermediate temperature range (approximately 130–160 K, depending on cluster size) at which the mobility is sufficient for effective exploration of the potential energy surface (PES), however low potential energy regions are still accessed preferentially. In this range, classical trajectories 'find' structures of particularly low energies. These structures are collected and subjected to further optimization, as described below. To account for the existence of such an optimal temperature range for accessing low energy minima, we recall the concept of solid/liquid phase coexistence in clusters, introduced by Berry *et al.* [129, 130].

In the second stage, optimization of H-structures is carried out for low energy minima found by classical trajectories. A Monte Carlo (MC) process is used which probes different orientational arrangements, for a given O-structure. (Typically, the trajectories do *not* produce an optimal H-structure for energetically favoured O-frames.) In particular, the pattern of surface dangling atoms, which affects

significantly the energetics [14, 15], is optimized at this stage. The MC algorithm was adopted from [13, 131], which addressed orientational ordering in ice. Since structural minimization is required at each MC step, this procedure was beyond our computational capabilities for the largest sizes, $n = 600$ and 931.

The third stage employed Rigid Body Diffusion Monte Carlo (RBDMC) [132]. Diffusion Monte Carlo is a method to solve the time independent Schrödinger equation by random walk of a cloud of replicas of a system [133, 134]. In the long time limit, the distribution of replicas in space approaches the ground state wave function. Here, RBDMC serves as a tool for structure optimization. Advantage is taken of the tendency of the replicas to drift towards low PES regimes. RBDMC was combined with a computational device of PES smoothing, i.e., replacement of the true potential energy by the energy of the nearby minimum, as in the basin hopping algorithms [135]. The potential energy surface is thus smoothed to a sequence of flat-bottomed wells, and the potential barriers are eliminated. Such smoothed PES was used by Wales and Hodges in conjunction with classical Monte Carlo, in a search for global minima of water clusters up to $n = 21$ [75]. The present version of DMC-based optimization was found useful for final structural adjustment of relatively flexible clusters, at sizes of tens of molecules.

The project was computationally intensive, and therefore the computationally efficient TIP4P potential [114] was employed. For low-lying minima of $n = 21$, and for select minima of other sizes, energy trends were double-checked against the polarizable TTM2-R potential [136]. While the gross energy trends appear consistent for the two potentials, there is disagreement in the detailed energy ordering. TTM2-R is likely to be more accurate than TIP4P; however we suspect that none of the presently available empirical or *ab initio* models is sufficiently accurate to predict the exact energy ordering for the pertinent sizes.

In the following analyses, two molecules were defined as hydrogen bonded if the minimal O···H distance was less than 2.5 Å, except for the results of table 1 for which a somewhat shorter cutoff of 2.3 Å was used.

2.2. *Structural optimization: results*

The problem of a judicious choice of input configurations arises in connection with the question of our main interest – the onset size for crystallinity. There are select cluster systems such as NaCl, which crystallize easily in the course of the optimization [137] (and references therein). Unfortunately, H_2O does not belong to this category, most likely due to a high nucleation barrier. Water freezing was successfully observed by Ohmine *et al.* in a simulation with periodic boundaries, at a very high computational cost [138]. Two preceding studies demonstrated crystallization in simulations assuming a strong external electric field [139–142].

A more limited approach was adopted by us. Optimization was applied to initially amorphous structures ('frozen droplets'), and also to initial structures cut out from a known crystal (ice Ic); and the results were compared. For $n = 48$ and 123, the crystallinity was *lost* in the course of the optimization of initially crystalline structures; moreover final energies and structural characteristics were similar to those obtained using amorphous initial conditions. The lowest energy structures found starting from both types of initial conditions can be described as compact and amorphous (figure 1). Thus the crystallization threshold size appears to correspond to $n > 123$.

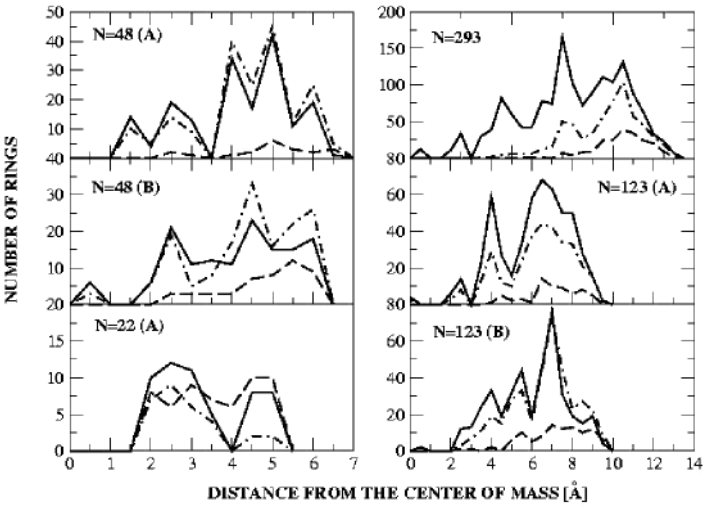

Figure 8. Distribution of ring sizes, as a function of distance (in Å) of a ring centre to the cluster centre-of-mass, for lowest energy cluster structures shown in figure 1. For $n = 48$ and 123 results for an additional low energy structure (B) are shown to demonstrate the variability of the results. Structures (A) were obtained from optimization of structures cut from a crystal, while nearly isoenergetic structures (B) were derived from amorphous initial conditions [23]. Thick solid line: six-membered rings; dot-dashed: five-membered; dashed: four-membered.

On the other hand, for initially crystalline $(H_2O)_n$ structures with $n \geq 293$, the crystal structure of the cluster core survived the optimization, and the resulting final energy was lower than that obtained from initially amorphous structures. For $n = 293$, 600 and 931 the lowest energy structures found were spheroid, with a crystal core and a disordered surface. At $n = 293$ (figure 1), the core is composed of a small number of six membered rings, which are distorted by interaction with the disordered surface. At $n = 931$ (figure 2), well crystallized ice is present in the interior. (The outer part of the predominantly crystal core is still strained by interaction with the surface; the effect on the spectra will be discussed in Section 3.)

The spheroid shape allows for minimization of the surface area, but is inconsistent with crystal surface structure. Structural optimization of initially fully crystalline structures is associated with enhancement of the population of five- and four-membered water rings in the cluster surface, which allows for reduction in the population of undercoordinated molecules. (The five- and four-membered water rings are absent in a crystal.) A distribution of ring sizes for $n \sim 20$–293 is shown in figure 8. It is seen that for $n \leq 123$, rings with less than six water molecules permeate the entire cluster volume, reflecting the amorphous cluster structure. At $n = 293$, a small crystal core is present, dominated by six-membered rings.

In addition, for $n = 48$, we examined several 'special' ordered structures, generated manually – a perfect tube made of stacked four- and six-membered rings, and a perfect near-circular sandwich composed of fused six-membered rings [23]. All these structures yielded significantly higher energies than the lowest energy amorphous compact structure shown in figure 1; this result was double-checked with the TTM2-R potential. While these 'special' structures correspond to enhanced percentage of 4-coordinated molecules, as compared to the optimized amorphous

structures, strong deviation from the tetrahedral bonding raises the energy of the former with respect to the latter. This finding underscores the notion that the quality of the hydrogen bonds, not only their quantity, affects significantly the energetics.

2.3. *Calculations of spectra*

2.3.1. *Method*

For the above structures, the spectra were calculated quantum-mechanically using a model developed by us in the past [27, 143, 144], which incorporates elements from a number of studies by other authors [62, 145, 146]. (Molecular dynamics calculations of spectra are problematic due to artifacts of the classical treatment of high frequency modes with $\hbar\omega > k_B T$; see, e.g., [147].) The model was calibrated originally for H_2O and D_2O ice, and for isotopic ice mixtures [24, 143]. The OH bonds are treated as local Morse oscillators [62, 145]. The ground state is approximated as a product of ground Morse states for all the OH bonds. An excited state is expanded in the exciton basis $\sum c_i|1_i\rangle$, where $|1_i\rangle$ is a product basis state with one quantum in bond i, and zero quanta in the remaining bonds. The intermolecular OH$\cdots$OH coupling is modelled as oscillating dipole–oscillating dipole interaction [27, 146]; interaction centres are placed near OH midpoints.[1] The intramolecular coupling is a sum of momentum coupling between two OH bonds sharing an O-atom ($p_1 p_2 \cos(\mathrm{HOH})/m_o$ [148]), and a potential coupling which is bilinear in bond displacements $k\delta r_1 \delta r_2$ ($k = 0.0385\,\mathrm{mdyn/\AA}$). In accord with past analysis of spectra of D_2O isotopically isolated in H_2O ice, oscillating dipoles were assumed to be directed along OH bonds [149], with a dipole-derivative value of 4 Debye/Å [150].

Further extensions were necessary for treatment of water clusters and ice surfaces, which include both dangling and bonded OH, and a range of hydrogen-bond strengths. For these systems, one must include the dependence of OH vibrational properties on hydrogen bond configuration. It is known that the OH stretch frequency drops by hundreds of cm^{-1} upon formation of a strong H-bond. Moreover the bond force constants depends sensitively on hydrogen bond geometry, as indicated, for example, by a $\sim 450\,\mathrm{cm}^{-1}$ frequency difference between the bonded-OH band of 3-coordinated molecules with a d-H, and the OH frequency of 3-coordinated molecules with a d-O [104, 144]. Bond dipole derivatives are also highly sensitive to hydrogen bonding; the integrated absorptivity of the stretching vibrations of water vapour is smaller by factor 28 than that of ice I at 100 K [149].

Our treatment of the OH frequency dependence on H-bonding was inspired by *ab initio* studies of [151], which suggested a parabolic dependence of OH frequency on the electric field component $E_{||}$ along the OH bond, at the H-atom location. We generalized this idea, and calibrated a monotonically decreasing function $\omega(E_{||})$, where ω denotes the decoupled bond frequency, and the electric field is calculated using an empirical potential at the minimum energy configuration. The model was used quite successfully for the interpretation of size-selected water cluster spectra

[1] Best agreement with experiment was obtained by placing the centre of interaction on the OH bond axis, at a distance 0.62 Å from O [27].

in the size range $n = 7$–10 [104].[2] Calibration of $\omega(E_{||})$ was made using comparison of experimental and computed spectra for $(H_2O)_8$, and for $(H_2O)_{931}$ [21, 22, 104]. Since $\omega(E_{||})$ was calibrated for rigid-body polarizable potential EMP [13, 105], the cluster structures obtained in the optimization study (which employed TIP4P) were re-minimized with EMP prior to spectrum evaluation. More detailed discussion of the method for spectra calculation can be found in Section 3 of [106] (except that there, a more elaborate model was used which includes the effect of the intermolecular zero-point motion on the OH-stretch spectra).

The OH bond dipole derivative μ' is known to increase strongly with the redshift in the OH frequency. Following combined *ab initio* and Monte Carlo results of [152] for liquid water, and our studies of ice surface spectra [144], linear dependence was adopted for $(\mu')^2$ on the bond frequency: $\mu' = 0.756[1 + 0.0655(3715 - \omega_i)]^{1/2}$, where the result is in D/Å. The parameters were calibrated using the experimental ratio of the integrated bonded-OH intensity to the free-OH intensity; that is, this ratio computed for the $(H_2O)_{931}$ cluster was brought to agreement with the one measured for particles of 4 nm mean diameter [21].

The infrared absorption intensity to an excited state is proportional to $I = (E_{\text{exc}} - E_{\text{gs}})|v|^2$, where E_{exc} and E_{gs} denote excited and ground state energies [148], and the body fixed components $k = x, y, z$ of the transition dipole v are calculated as $v_k = \sum_i c_i e_{ik} \mu'_i \langle 0|\delta r_i|1\rangle$; where e_{ik} denotes a projection on axis k of a unit vector along ith bond, and μ'_i the corresponding bond dipole derivative. Thus, the bond dipole derivative is assumed to be directed along the OH-bond. In reality, this is true for crystal ice; whereas in gaseous water, the bond derivative is directed 25.2° outside the bond [149]. The variation of the oscillating dipole component orientation, as a function of molecular bonding geometry, is an interesting unanswered question. In particular, more accurate calculation of surface contributions to the spectra would require detailed information on the dependence of the dipole derivative with respect to bond stretch on H_2O bonding configuration, particularly for undercoordinated molecules.

The spectra were averaged over three perpendicular polarization directions. The transitions to the individual excited states were assigned widths of $30/15\,\text{cm}^{-1}$ in the bonded/free-OH spectral regions. For the smallest cluster sizes investigated, the calculated lineshapes corresponding to individual minima are more structured than the experimental ones (compare figure 7 to figures 4 and 5). In the experimental spectra, features originating from specific molecular arrangements are averaged out by presence of numerous minima, and by the size distribution. To account partially for this effect, the calculated spectra for $n = 20$–293 shown in figures 3 and 6 (which were used in the interpretation of the experiments) were averaged over 10 lowest energy configurations found for each size. Accurate treatment of averaging over structures corresponding to a given set of experimental conditions would require a separate in depth study.

[2] Later, extension was made to include the effect of intermolecular vibrational averaging on the electric field. The potential minimum is a 'special' point at which the hydrogen bonds are particularly strong, and the electric fields are particularly large. The averaging was included, to account for delocalization due to zero-point and thermal intermolecular motions, and to represent temperature dependence of the cluster spectra [105–107]. However these averaging effects are not included in the present study, which focuses on fairly large and computationally expensive clusters.

2.3.2. *The computed spectra*

The calculated spectra are shown in figures 3 and 6, together with experimental spectra in figures 4–6. (Figure 6 displays the calculated surface contribution to the spectra.[3]) While the agreement is far from perfect, the scheme appears sufficiently accurate for qualitative interpretation. The experimental spectra, as well as comparison between theory and experiment, will be addressed in detail in the following sections. Meanwhile, qualitative features of the computed spectra are discussed briefly. The discussion is aided by decomposition of spectra to contributions from different H_2O coordinations, shown in figure 7.[3]

The smallest clusters, with $n = 20$–22, include 50–60% of 3-coordinated molecules, which are therefore major contributors to the spectrum. The 3-coordinated molecules with a d-O dominate the high frequency wing of the bonded-OH band; it appears that the need to accommodate both OH in the surface hydrogen-bond network results in particularly weak hydrogen bonds. The d-H molecules contribute the free-OH band at $3700\,cm^{-1}$, while the 'companion' bonded-OH absorbs at the low frequency end of the spectrum; thus the optimization of the H-bonding geometry by the 'companion' OH of d-H molecules is particularly effective. The 4-coordinated contribution appears between the d-O and the 'companion' frequencies, and overlaps with them to some extent at the edges.

Transition from $n = 20$–22 to $n = 48$ marks the growth of the 4-coordinated H_2O contribution; 4-coordinated molecules now constitute ~60% of the cluster. Note the relatively large width of the 4-coordinated spectrum, and its extension to lower frequencies as compared to $n = 20$–22; appearance of lower frequencies is related to reduction in H-bond strain with increasing size. The large width is due in part to substantial intermolecular coupling, as evidenced by comparison to the narrower 20% HDO/80% D_2O spectrum of $n = 48$, in which the OH···OH coupling is reduced. In the latter spectrum, the respective contributions of the three coordinations to the bonded-OH spectrum are quite well separated.

In the larger clusters, the 4-coordinated molecules dominate the spectrum, constituting 81% of the cluster at $n = 931$. A clear shift in peak frequency is apparent between $(H_2O)_{123}$, which is amorphous, and $(H_2O)_{600}$, which is largely crystalline (see figures 3 and 7). The intermediate $(H_2O)_{293}$ spectrum is remarkably broad, with frequency range covering both that of $n = 123$, and that of $n = 600$ and 931. As discussed above, $(H_2O)_{293}$ corresponds to appearance of a strained crystal core in the optimized structure. In the larger clusters, d-O still dominates the high frequency wing of the $(H_2O)_n$ spectrum; however the 'companion' bonded-OH band of d-H molecules is now buried under the 4-coordinated contribution. The 20% HDO spectrum of the $n = 600$ cluster is again significantly narrower than that of the all-H_2O cluster.

Interestingly, the high frequency end of the 4-coordinated contribution to the spectrum is dominated by molecules donating protons to 3-coordinated d-H neighbours (figure 7, dot-dashed curves). Thus d-H molecules tend to form strong

[3] In the squared expression for intensity, there are cross-terms including contributions of molecules of different coordinations. In figure 7, each coordination was assigned half of such a contribution. Similar division was used to calculate surface contribution to the spectra in figure 6; that is, half of each surface-interior cross-term was assigned to the surface.

H-bonds as proton donors (via 'companion' OH) , and weak H-bonds as proton acceptors.

3. FTIR spectroscopy of 2.3–40 nm diameter (~200–10^6 molecules) ice particles

Here we address the characteristics of ice particles, in the 200–1,000,000 molecule range, as evaluated from spectroscopic data for ice aerosols and 3-D arrays of ice nanocrystals. FTIR spectra of bare and adsorbate-coated nanoparticles, combined with computed spectra for clusters in the ≤4 nm range, have been used to establish several basic properties of ice particles. Properties addressed include particle structure, surface structure, structural dynamics and the interactions of the surface with varied adsorbate molecules [22]. Initially attention will be directed to the methods used for FTIR sampling of ice particles, including techniques used to determine the average particle size for an array or aerosol. Knowledge of mean particle size is essential to obtain full value from the observed spectra, i.e., to determine the origin of variations in spectra with sampling conditions; the dependence of particle structure and surface structure on particle size; the variations in adsorbate–surface interactions and reaction rates with particle size. Discussion of size effects will be followed by a review of FTIR methods that permit separation of particle spectra into components of the surface, subsurface and core. A description of the surface structure, deduced through comparisons of simulated and experimental spectra, and its influence on interactions with strong adsorbates, in particular ammonia and hydrohalic acids, will be included. It should also become clear that observations of effects of certain adsorbates on ice-particle spectra add to the understanding of the ice surface, thus facilitating the understanding of interactions with adsorbates in general.

Much of this section will highlight an evolving concept of the surface of ice nanocrystals. The size of the particles under discussion guarantees that a significant fraction of the water molecules are a part of either the particle surface or subsurface. At 4 nm diameter, a size favoured here because both the computational and FTIR methods are fully applicable, roughly 60% of the molecules are in the surface layer. While this drops to ~6% at 40 nm, infrared absorption by surface molecules remains a significant and usable component of the FTIR spectra. The results for the larger nanocrystals are expected to relate most directly to the properties of macroscopic ice while insights to the properties of smaller particles may be useful in studies of large water clusters, in the 100–300 molecule range. In considering the ice surface spectroscopy, we follow the chronological order of recent particle investigations, beginning with the methods and results for larger particles, 16–40 nm in diameter. Extension of results to smaller nanocrystals, in the 4–12 nm range, will then be described. Finally spectra for particles 2.3–4 nm in diameter will be considered in terms of the relationship to the spectra of even smaller particles, addressed in Section 4. Of particular interest is a serious alteration of both particle surface and subsurface structure/spectra below ~3 nm that can be related to the absence of a crystalline core [22, 24].

3.1. *Methods of preparation and sizing of ice nanoparticles*

The spectroscopic methods that are emphasized here cannot be used to distinguish the cubic from hexagonal structure of ordinary ice; but it is likely that particles, formed much as for the electron microscopy studies [120, 121], are mainly

single crystals, each with a cubic ice core. Methods are described, for sample preparation and determination of average particle size, of either aerosols or 3-D arrays, ranging up from ~2.3 nm in diameter.

3.1.1. *FTIR sampling of ice nanoparticles*

The focus is on the formation and spectroscopy of ice particles of average diameter 2.3–20 nm with limited results included for particles as large as 40 nm. The particles are formed by rapid expansion of a 0.1–1.0% premix of water vapour with an inert gas (usually helium or nitrogen), held at pressures in the 10–300 torr range, into the cold inner cell of a double-walled metal FTIR cluster cell. Typically, the expansion is accompanied by a pressure drop of 30–50%. A cartoon view of a sample cell, cooled by an Air Products 202 closed-cycle helium refrigerator, with ZnS inner windows sealed to the cell body by indium gaskets, is given in [155]. Though much smaller and simpler, such collisional cooling cells generally resemble one first described by Ewing [156].

The inert carrier gas provides for rapid collisional cooling of water molecules, causing aggregation on a subsecond time scale. This produces (spherical) nano-droplets of a size largely limited by two factors; the droplet nucleation rate and the total available water vapour. The droplets then crystallize by homogeneous nucleation while cooling rapidly below 230 K. The astonishing nucleation rate of cubic ice, as determined from time-dependent electron diffraction of large water clusters in supersonic expansion beams [7–10], assures that the cubic phase is favoured by the particles of the aerosol. However, we shall see that an amorphous phase is obtained when the water vapour density is so limited that an average particle is $\leq$2.6 nm in diameter.

The determination of size, as described in the next subsection, has provided information about the relation of particle size to sampling conditions. Small size is favoured by low cell temperatures (i.e., faster droplet nucleation and reduced Ostwald ripening), reduction of water vapour content in the gaseous premix, a low cell load pressure and the use of helium as the carrier gas. Examples of average particle size for particular sampling parameters are: 2.6 nm for 12 torr loads of 0.3% water in He (g) into a 40 K cell; 16 nm for 300 torr load of 1% water in He (g) at 70 K; 40 nm for 300 torr load of 1% water in N_2 (g) at 140 K. Because small particles are lost to Ostwald ripening (accelerated by higher T) and larger particles to rapid settling (enhanced by lower T), there usually exists a temperature for a given gas pressure at which the average particle size remains constant with time while the ice absorbance is steadily reduced by particle settling. The half-life of an ice aerosol typically falls in the range of 4–20 min as determined by several interrelated factors: particle size, cell temperature and cell pressure. Also, the increasing particle vapour pressure with reduction in particle size (Kelvin effect) generates a size-limiting rate of Ostwald ripening; so that, in effect, there is a minimum average particle size that increases with temperature (e.g., temperatures below 40 K are required for particles smaller than ~2 nm; see Section 4). This minimum size may be further influenced by an increasing number of agglomerate-producing collisions at higher temperatures [153].

A variety of useful spectroscopic measurements are possible while employing ice aerosol samples. For example, because ice refines itself through the ejection of most foreign molecules as it crystallizes, it is possible to prepare an aerosol in which the crystalline particles, as formed, are coated to a selected level by many different types

of adsorbates [22]. Hydrophobic substances are similarly forced to the surface of smaller amorphous water clusters. However, the limited lifetimes of the aerosols, and the difficulty of exposing aerosol particles to a reactant species in a controlled manner, does prohibit certain studies, e.g., the kinetics of the conversion of ice to hydrate particles. Most of these limitations have been overcome by sampling with 3-D arrays of ice nanocrystals [155, 157]. Such arrays are a natural consequence of the cycle of loading and pumping of an aerosol from the cold cell. Depending on the cell temperature, as much as 5% of the aerosol particles are left on the cell windows during each cycle; so that an array of a desired optical density can be prepared by cycling several times. The network of ice particles that make up the arrays is surprisingly stable; the FTIR spectrum is unchanged by time (weeks) at low temperatures or by pulsed cyclic exposure to inert gas pressures of 0.5 bars. (It is likely that the arrays are formed from smaller networks of ice nanoparticles generated by particle aggregation in the aerosol phase [153].) An ability to follow slow structural relaxations within particles of the 3-D arrays, associated with Ostwald ripening or interactions with adsorbates, has been critical to the determination of spectra of the ice surface and subsurface ([158] and Section 3.2).

3.1.2. *Ice particle average size determination*

Because the ice nanoparticles are formed by droplet crystallization, the particles approximate a spherical shape; as confirmed by electron microscopy, which has also provided a rough indication of size distributions of particles formed by collisional cooling [120, 121]. For such particles, the ratio of surface area to volume varies as the inverse of the diameter. The volume is proportional (roughly) to the integrated intensity of the bonded-OH band. Our first approach to estimate the surface area consists of covering the clusters by a monolayer of adsorbate, and measuring the corresponding spectra.

The CF_4 molecule has been identified as an ideal adsorbate with which to establish the total surface area of an ice aerosol or array by FTIR methods [18]. The triply degenerate asymmetric-stretch mode of CF_4 is characterized by a very large dipole derivative. Spectra of collections of molecules with large dipole derivatives are known to be highly sensitive to sample geometry [159–161]. Large dipole–dipole coupling exists between oscillations of different adsorbate molecules, resulting in collective excitations. Two types of modes correspond to particularly large infrared absorption intensity – the high frequency in-phase modes which are polarized in the direction perpendicular to the surface, and the low frequency in-phase modes polarized parallel to the surface. The two types are denoted 'longitudinal-optical' (LO) and 'transverse-optical' (TO) modes, respectively [159–161]. The corresponding measured and computed adsorbate spectra are shown in figure 9; for further details, see [18]. The current sizing method relies on the fact that the 'LO-TO' splitting depends on the coverage, and maximizes near $78\,cm^{-1}$ for **monolayer** CF_4. As is clear from the experimental and simulated spectra, coverage beyond a full monolayer causes the emergence of a broad intermediate absorption, while the splitting of the components of the doublet decreases for either submonolayer or multilayer coverage. At reduced coverage, splitting decreases due to reduced coupling; while at increased coverage, splitting decreases due to reduced CF_4 sample asymmetry in the two polarization directions. Thus, monolayer coverage of CF_4 on particles of an ice aerosol, or of a 3-D

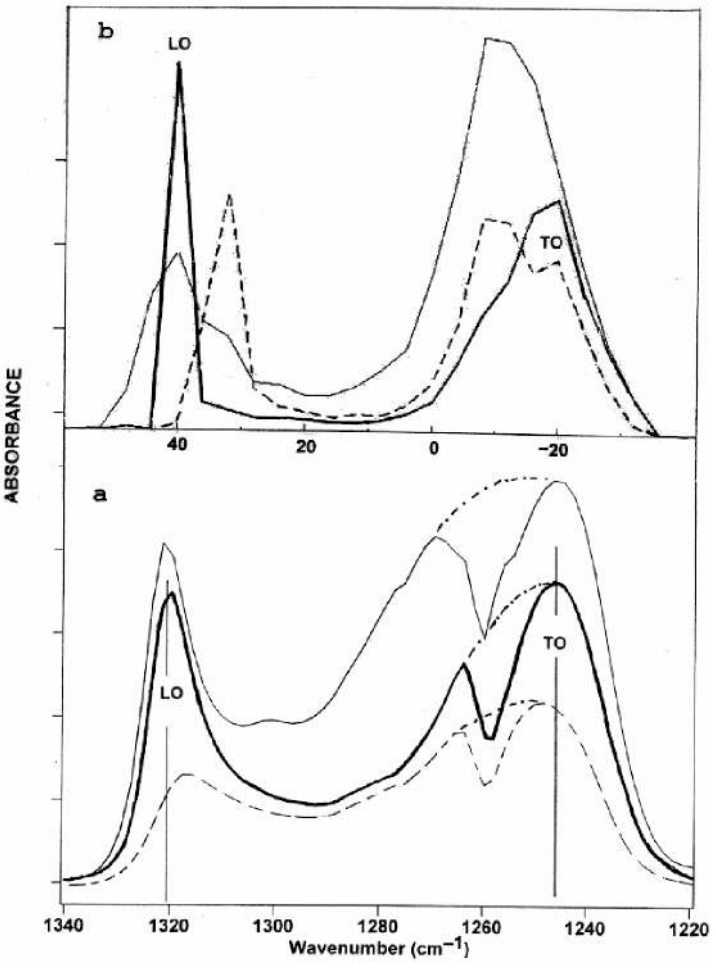

Figure 9. Experimental (*a*) and simulated (*b*) spectra of CF_4 near-monolayer (ML) coatings on 'spherical' surfaces: (*a*) coatings of $<$ ML (dashed), $\sim$ML (bold) and $>$ ML (thin) on $\sim$6 nm average diameter ice particles. The dot-dashed lines are to aid viewing by elimination of the Evans hole at 1260 cm^{-1} in the experimental spectra. The computations (*b*) pertain to CF_4 molecules randomly distributed in a spherical shell of $\sim$5 nm diameter; thick solid – a fully packed 1 Å thick shell with 339 CF_4 ('monolayer coverage'); dashed – 1 Å thick shell with 280 molecules ('submonolayer coverage'); thin solid – 2 Å thick fully packed shell, with 638 CF_4.

array, can be recognized and used in the determination of particle size. One may note that the CF_4 lineshapes are also highly sensitive to the extent of molecular disorder, and were used in the past to demonstrate the disordered structure of the ice nanoparticle surface [18].

The absolute intensity of the CF_4 mode is known and is quite stable for different phases [162]. So the integrated band intensity of the mode for a monolayer coating of the particles of an ice nanocrystalline sample can be converted into the total surface area of the sample provided the surface area per CF_4 molecule is known. That area can be estimated from the simulation of ice coated with CF_4 [18]; which indicates one CF_4 molecule for each pair of surface water molecules; i.e., the CF_4 area per molecule is that of a hexagonal ring in the case of the basal plane, and since each

water molecule is shared with three hexagonal rings, there are two molecules per ring. Further, the absolute intensity of the ice OH stretch band in the 3300 cm^{-1} region is also known [150], so the measured ice band can be used to estimate the total ice volume of a particular sample. With the surface area known from the CF_4 intensity, and the volume known from the ice band intensity, the average particle size can be estimated. However, such an approach ignores the fact that, when the average size is quite small, a significant fraction of the molecules (those in the outermost layer) do not contribute proportionately to the ice band intensity. In actual practice, the number of surface water molecules is obtained from the CF_4 band intensity, while the number of **interior** water molecules is deduced from the ice band intensity. Interior molecules are considered those fully coordinated molecules not part of the surface, so the surface contribution to intensity must be removed from the total intensity to estimate the interior intensity. In this step, it is presumed that the absolute intensity of the outermost molecules of reduced coordination, although significant, is small while that of the fully coordinated molecules is less than, but similar to, that of the interior. Since half or more of the surface molecules are 4-coordinated, the surface intensity component is removed from the total by assuming that the average absolute intensity of the molecules of the outer surface is 50% that of the interior molecules. These measurements and assumptions yield a ratio for the number of surface-to-interior molecules, or the percentage of water molecules (X) that are surface molecules; information that can then be converted to particle size.

To convert this percentage to particle size requires a value for the thickness of the ice outer surface. This is often taken as ~0.3 nm though a somewhat thicker surface has been estimated from the fitting of simulated to experimental spectra of 4 nm particles [21]. To remain consistent with the concept that the outer surface is approximately a 'bilayer' thick, the surface thickness is taken here (solely for the purpose of size estimate) as 0.3 nm. Then the diameter, in nm, for a particle with X percentage of all water molecules in the surface, is $\sim 180/X$.

3.1.3. *Application of particle size information*

It is interesting to note how various properties vary with ice particle size as measured using methods described above. For example, one can evaluate the (relative) density of d-H molecules on the surface of ice as a function of particle size – a question of some interest since the d-H molecules constitute high energy reactive surface sites [163–169]. This question can be addressed as in figure 10 by plotting the dependence of the ratio of the monolayer CF_4 band intensity (i.e., the particle surface area) to the integrated intensity of the ~3693 cm^{-1} band of d-H molecules as a function of particle size. The ratio is constant at ~100 for particles larger than 5 nm, indicating a size-independent d-H density. However, a rapid **decrease** in density is indicated below 4.5 nm.

Similar evidence of a decrease in d-H surface density might be expected in a plot of the ratio of the ice-band integrated intensity to the integrated intensity of the free-OH band versus particle size as given in figure 11. However, the data points indicate a nearly constant slope of 150, suggesting a fixed d-H surface density for diameters ranging from 2.5 to 18 nm. However the points between 2.5 and 4.0 nm all fall above the 'line', hinting at a lower d-H density, and it must be kept in mind that the surface becomes a major contributor to the ice band intensity, for the smallest particles. The lower absolute intensity for the ice surface molecules would therefore suppress

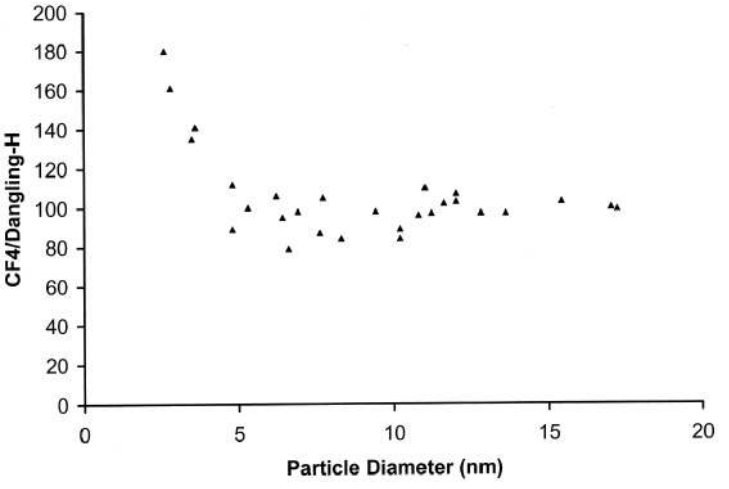

Figure 10. Dependence of the **ratio** of the integrated intensity of a monolayer of adsorbed CF_4 to that of the surface free-OH band on particle diameter.

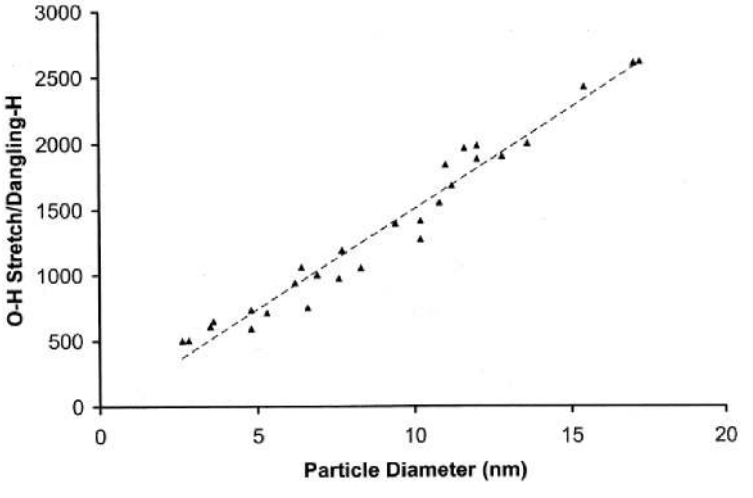

Figure 11. Dependence of the ratio of the integrated intensity of the main particle O-H stretch band to that of the surface free-OH band on particle diameter.

the value of the plotted ratio most strongly in the 2.5–4 nm size range. So figures 10 and 11 both indicate a reduced surface density of d-H molecules for ~4 nm or smaller particles. Further, the constant d-H density found for particles larger than 4 nm suggests that the ice surface structure changes little above ~4 nm; so results for surface studies of ice nanocrystals appear applicable to larger, and perhaps macroscopic, ice particles.

The plot of figure 11 can also be useful for estimating ice particle size for any aerosol or array for which the integrated intensity of the d-H and bonded-OH ice bands can be measured. However, d-H atoms should be unbonded to adsorbate, since the latter affects significantly the intensity; we shall return later to this point. Figure 12 shows the variation of other particle parameters with particle size; the values for the smallest *n* are taken from work described in Section 4. This graph

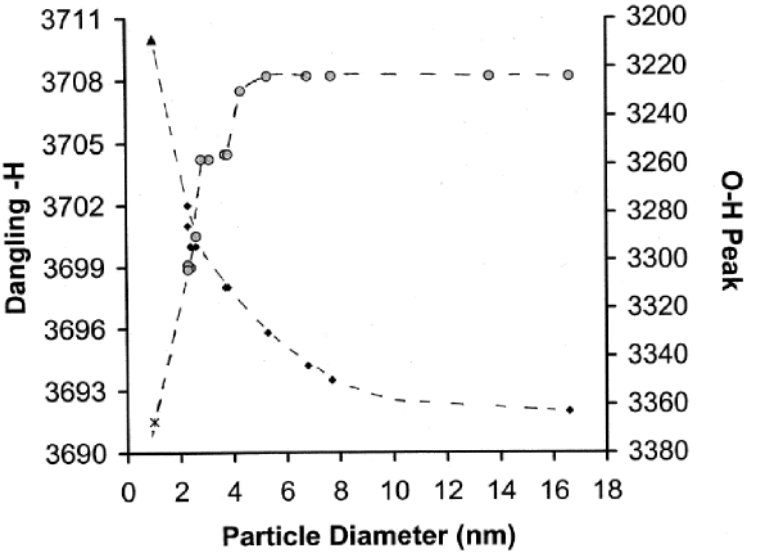

Figure 12. Variation of peak positions of the free-OH band (diamonds) and of the main hydrogen-bonded OH band (circles) with particle size. The triangle and asterisk denote points determined for ~1 nm water clusters with an adsorbed N_2 monolayer at 5 K. The d-H value was obtained by adding 8 cm^{-1} to the value for the bare 2.3 nm particle since that is the difference observed for the frequency when both the ~1 nm and ~2.3 nm clusters are N_2-coated, as in figure 5.

shows that the surface d-H-mode frequency increases rapidly below ~6 nm with peak positions shifting from 3692 to 3710 cm^{-1}. An accompanying rapid increase in the bonded-OH band peak position, from ~3220 to > 3350 cm^{-1} between 5 and 1 nm, is also apparent in this figure. The latter increase occurs in interesting stages: the peak frequency is nearly constant at ~3220 down to 5 nm, increases to ~3260 cm^{-1} and then remains nearly constant in the ~3–4 nm range, and proceeds to increase towards smaller sizes. The physical interpretation of these results, in terms of structural evolution of the clusters will be suggested in Section 3.3.

3.2. *Determination of the surface and subsurface spectra of ice*

Methods, based on relative relaxation rates, have been developed that reveal the surface and subsurface spectra of large (> 20 nm) ice nanocrystals within 3-D arrays. A different approach that invokes the predetermined large-particle subsurface spectrum is particularly useful with smaller ice aerosol particles (3–8 nm). Both approaches are based on the recognition that spectra of ice nanoparticles above the size of ~4 nm can be represented as a sum of three distinct recognizable components, designated as 'surface', 'subsurface', and 'well-crystallized interior'.

As discussed earlier, the nanoparticle surface is viewed here as 'reconstructed'. The reconstruction corresponds to recombination of excess dangling atoms of the particle surface, to form additional hydrogen bonds; the result is surface disordering, and also distortion of the underlying largely crystalline subsurface layer. (The reconstruction appears particularly effective for particles of diameter ≤4nm, as indicated by the reduced d-H density; see Section 3.1.3 above.) In determination of a valid surface spectrum by relaxation methods, it is essential that the presence of subsurface ice with a unique spectrum be recognized. Experimentally, the first

indication of a significant subsurface region was from **difference spectra** associated with particle growth by Ostwald ripening. If there were no subsurface, the net effect of ripening would be the conversion of surface ice to crystalline core ice as the average particle size increases. The difference between spectra taken before and after ripening would then reflect only the loss of surface and the gain of crystalline ice. Adding out the known crystalline ice component would then yield a unique surface spectrum. However, this procedure was found to produce markedly different surface spectra for different temperatures or periods of ripening; indicating the presence of a significant subsurface structure [158]. The relative contributions of the 'surface' and 'subsurface' components to the difference spectra can be thus varied by performing the ripening under different conditions; which enables determination of the two respective spectra.

The subsurface spectra can be determined alternatively by a method employing adsorbates [158]. The method relies on the fact, that the tendency towards surface reconstruction can be reversed by adsorbates. This is since unreconstructed surface contains excess undercoordinated H_2O molecules which now serve as effective binding sites; in addition, the nanoparticle hydrogen-bond network is improved due to release of strain. Sufficiently strong adsorbates cleave the (relatively weak) recombined hydrogen bonds; and the resulting partial 'surface de-reconstruction' leads to conversion of much of the spectroscopic subsurface contribution to the 'well-crystallized' interior spectrum. Differencing enables determination of the subsurface spectrum. The result matches the one obtained from Ostwald ripening. More details are given below.

3.2.1. *The surface/subsurface of 20 nm ice particles*

'Intermediate' adsorbates, such as H_2S, HCN, C_2H_2 and SO_2 have a qualitatively different and much greater effect on the ice particle spectrum than do weak adsorbates. For example, during the initial uptake of SO_2 at 120 K, three bands that match the peak positions of crystalline ice emerge in the difference spectrum versus that of the original bare ice. During a second phase, the peaks of the crystalline core ice continue to grow, but, even though the d-H sites of the ice surface were saturated with SO_2 during the first phase, a sizeable enhancement also occurs at the position of the SO_2-shifted free-OH band – 3610 (2670) cm^{-1} for d-H (d-D) of H_2O (D_2O) ice. Then, in a third phase, the crystalline ice peaks continue to strengthen but the d-H region is unchanged.

This sequence, which was observed for many different adsorbate-ice samples, is understood in the context of the basic ice particle structure model as follows. Because of lower signal-to-noise values in the O–H stretch region, the more reliable results obtained with D_2O ice are examined first. Most critical is the emergence of the extra intensity in the SO_2-shifted d-D band during the second phase. With the surface already saturated with SO_2, this intensity is indicative of a new source of d-D sites on the ice surface to bind with additional SO_2. The source can be anticipated by recalling that ice-surface reconstruction is accompanied by a pronounced decrease in 3-coordinated surface molecules through bonding of neighbour d-D and d-O groups [18]. Further, simulations show that the new H-bonds are weak and distorted and readily cleaved by adsorbates (NH_3, for example; see [170]). SO_2 can also cleave the strained bonds to gain access to the 3-coordinated water molecules thereby generated. Adsorbate insertion into weak H-bonds thus transforms the ice surface structure towards that of the unreconstructed surface, and, in doing so, reduces

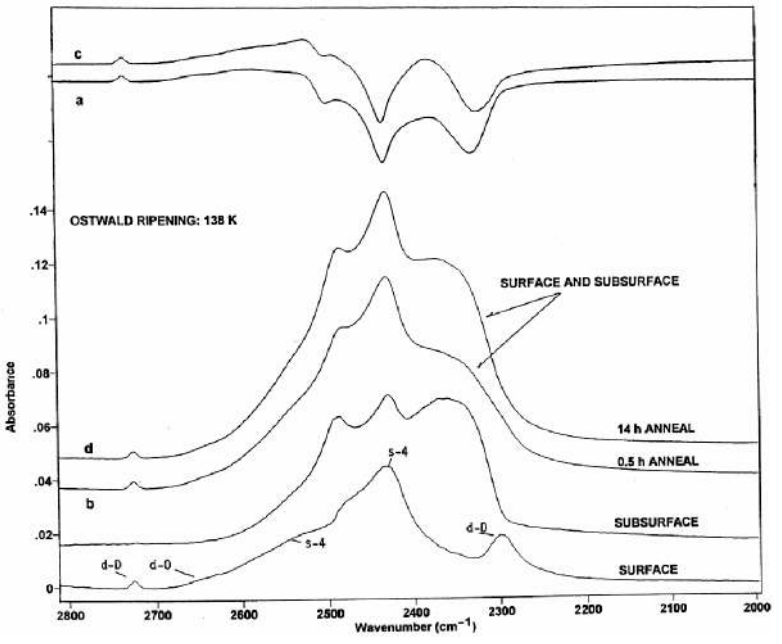

Figure 13. FTIR difference spectra for sequential periods of Ostwald ripening of ice nanocrystals at 138 K. Curves (*a*) and (*c*) compare before and after ripening for 0.5 and 14.0 h, respectively. Curves (*b*) and (*d*) are (*a*) and (*c*) with the ice core component removed. The surface and subsurface spectra are from differences between (*b*) and (*d*) as described in the text.

strain in the subsurface region. From this view, the third stage in the SO_2 interaction with the ice surface, during which there is no significant change in the intensity of the d-D band, corresponds to the relatively slow relaxation of the ice subsurface to crystalline interior ice. The difference spectrum, comparing before and after the relaxation, reflects this conversion; so removal of the crystalline ice component from the difference spectrum gives the subsurface spectrum an example of which is included in figure 13.

With the subsurface spectrum known from the relaxation induced by an adsorbate, difference spectra that reflect Ostwald ripening of the ice nanocrystals can be more fully analysed, the form of the subsurface spectrum further tested and the surface spectrum determined. Ripening must ultimately convert both surface and subsurface molecules to crystalline core molecules since the amount of surface and subsurface both decrease with increasing particle size. However, the relaxation of the mostly 4-coordinated subsurface molecules to steady state positions is much slower than that of the more mobile surface. An initial ripening period, at some elevated temperature, thus gives primarily a net surface-to-interior conversion, whereas longer periods of ripening at the same temperature produce relatively more subsurface loss [158]. This can be seen in figure 13 in which the **difference spectra** for two greatly different periods of ripening at 138 K are shown in curves (*a*) and (*c*) which were determined at 120 K. Adding out the increase in interior crystalline ice gives curves (*b*) and (*d*) of which (*d*), from the long ripening period, resembles that of the subsurface (but clearly, from the presence of the d-D band, contains a surface component as well). Since the two spectra contain different portions of the surface

and subsurface components, subtracting one from the other can reveal each spectrum in turn. If (*b*) is subtracted from (*d*), using the factor required to null the $2726\,cm^{-1}$ d-D band of the surface, a subsurface spectrum appears, which matches closely the subsurface spectrum from adsorbate-induced relaxation. If this spectrum is then subtracted from either (*b*) or (*d*), or, if the right amount of (*d*) is subtracted from (*b*) the surface spectrum is obtained. Figure 10 of [158], shows the separation of spectra (*b*) and (*d*) into the two components. The resulting surface and subsurface spectra are included at the bottom of figure 13.

3.2.2. *The surface/subsurface of 4 nm ice particles*

The surface spectrum can also be revealed in a more straightforward approach that works particularly well for small nanocrystals (3–8 nm) for which the core spectrum is not so dominant. With both the subsurface and core ice components known from the larger particle spectra, subtraction of the correct amounts from a single spectrum of ice nanoparticles leaves only the surface spectrum. Here, as in the other procedure, there is subjectivity in recognizing the 'correct' subtraction factors. However, since this procedure can be applied to aerosols with a considerable range of particle size to yield the 'same' surface spectrum, the subjective factor is seemingly not serious [21, 125].

The 4 nm crystalline ice particle was chosen for particular study since (a) initial spectroscopic results, as well as the earlier electron diffraction measurements [5, 6], indicated that such particles are sufficiently large to have a crystalline core, and (b) a 4 nm particle is sufficiently small to permit thorough modelling using empirical potential functions (see Section 2 and figure 2, for $n = 931$). Though 4 nm particles were chosen for the direct comparison of experimental and computational results, the experimental determination of surface/subsurface spectra included aerosols of nanocrystals with average diameters ranging from 3–12 nm. The effect of the decreasing size on the particle stretch-mode infrared spectrum is apparent from figure 4 as determined for ice aerosols formed at 100 K from mixtures of H_2O in He(g). For both the H_2O [125] and the D_2O [21] series it was established that, for particles <10 nm and >3 nm in diameter, subtraction of the crystalline-core spectrum generates an invariant residual spectrum (bottom of figure 4). This residual spectrum was assigned to the composite spectrum of the surface and subsurface components of the particles. Thus, subtraction of the known subsurface spectrum (the H_2O equivalent of that of D_2O in figure 13) from the combined surface and subsurface spectrum gave the H_2O ice surface spectrum (figure 14(*b*)).

Together with the known subsurface and interior ice spectra, the surface spectrum was found to fit experimental spectra with minimal residual errors for particles ranging in size from 3 to ~12 nm. However, it should be emphasized that, from the nature of the process used to identify the subsurface component of the particle spectra (see Section 3.2.1), the two spectra reflect relative relaxation rates of local structures more directly than any geometric positioning of the molecules; the more rapidly relaxing near-surface structures are included in the surface spectrum. This definition of the 'surface' includes more near-surface molecules than the definition deduced for large water clusters in Section 3.1.2, giving a surface layer of ~5 Å in thickness [21].

The experimental spectra of the surface, subsurface and interior of 4 nm H_2O nanocrystals are compared in figure 14 with the simulated spectra of the 4 nm $(H_2O)_{931}$ particle. The simulated spectra of each of the three components of the ice

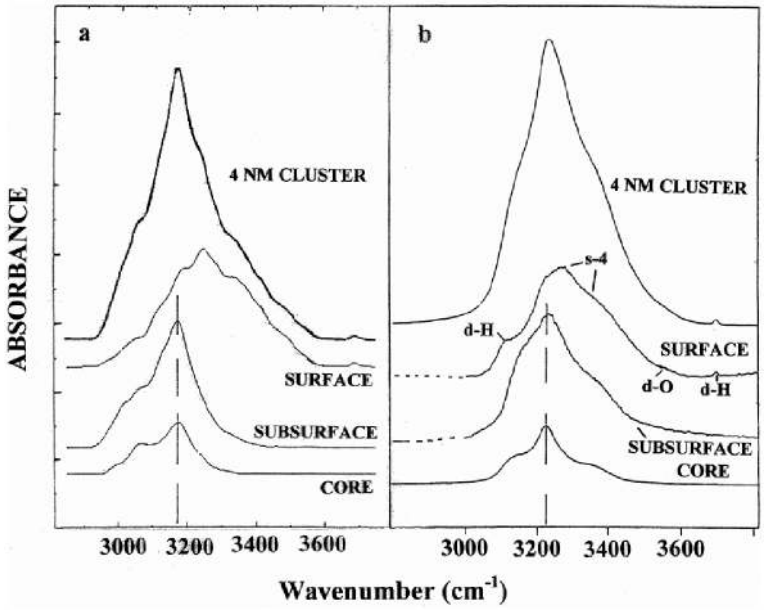

Figure 14. Simulated (*a*) and FTIR (*b*) spectra of 4 nm H_2O ice crystal(s). Core, subsurface, and surface components of simulated and experimental spectra are compared, and the assignment of subbands of the surface spectrum (based on that comparison) indicated.

nanocrystal match the experimental component spectra in a semiquantitative manner in terms of band positions, intensity and width. In addition to confirming the general concept of the structure of an ice nanoparticle, i.e., an ordered core, a strained/distorted subsurface and a disordered-surface, the simulated spectra permitted the credible assignment of the various subbands of the surface spectrum, as indicated by labels in the figure. The results also advanced the identification of particle sizes through the use of the relative intensities of the surface, subsurface and core components of the 4 nm case as a reference state.

The complexity of the various spectra of H_2O (or D_2O) ice particles is enhanced by the strong dipole coupling of the molecular-stretch modes common to the condensed phases of water [27, 146]. This diminishes the value of the position of the subbands of the component spectra as a measure of the strength of individual H-bonds. This problem was overcome in [21] by a computational approach in which a 4 nm particle was composed of only HDO molecules with no coupling between bonds. The computational results were then compared with 'decoupled' experimental spectra for ~18% HDO molecules isolated in H_2O nanocrystals. As for the H_2O particles in figure 14, the computed spectra matched the experimental spectra of 4 nm particles in a semiquantitative manner, giving an assignment for the features of the surface spectrum while strengthening the tie between band positions and specific H-bond strengths.

3.3. *Connection between spectroscopic and structural evolution with size*

Here, molecular level interpretation is pursued for the above spectroscopic results, with the help of computational models.

Table 1. Mean values (standard deviations) for O···O distances of hydrogen-bonded molecules, and for O···O···O angles between adjacent hydrogen bonds. Two molecules were defined as hydrogen bonded if the minimal O···H distance was less than 2.3 Å

n	$r_{O\cdots O}$ Å	O···O···O degrees
931(int)[a]	2.700(0.007)	109.4(3.7)
931(sub)[a]	2.703(0.019)	109.2(7.7)
931(surf)[a]	2.747(0.046)	108.0(17.1)
293('sub')[b]	2.703(0.021)	108.9(13.2)
293('surf')[b]	2.737(0.040)	107.5(18.1)
293	2.733(0.039)	107.7(17.5)
123('am-core')[c]	2.713(0.021)	108.2(15.2)
123('am-surf')[c]	2.734(0.034)	106.2(18.5)
123	2.732(0.034)	106.7(17.8)
48	2.735(0.035)	105.4(17.9)

[a] In $n = 931$, the distances from cluster centre-of-mass, corresponding to boundaries between core, subsurface and surface were set to 9 and 14 Å, as in [21]. The three respective categories include 11%, 30% and 59% of molecules, respectively. See also distribution of molecular distances from the cluster, shown in figure 24.
[b] In $n = 293$, the crystal interior is of small spatial extent, and strongly stretched by the interaction with the surface (figure 1). The boundary between 'surface' and 'subsurface-like core' was set here at 6 Å from the cluster centre-of-mass; this distance corresponds to a core dominated by six-membered rings, which includes ~10% of the molecules [23].
[c] In $n = 123$, both the core and the surface are amorphous; the boundary was set at 5 Å from the cluster centre-of-mass, at a depth of ~5 Å from the cluster surface (this depth is similar to the one used for the definition of 'surface' for the larger clusters).

Figure 2 shows an inner slice of the 4 nm (931 molecule) model cluster. In the computed spectra of figure 14, the molecules were assigned to 'interior', 'subsurface' and 'surface' according to their distances from the cluster centre-of-mass; the best agreement with experiment was obtained using separation distances of 9 and 14 Å for the three categories (marked by circles in figure 2). As noted above, the corresponding surface layer corresponds to the thickness of ~5 Å. It is seen that the ~5 Å thickness includes the non-crystalline component of $n = 931$. (Figure 8, which was adopted from [23], shows the distribution of ring sizes within the clusters in the size range $n = 22$–293. Recall that ice crystal structure is dominated by six-membered rings, and therefore smaller rings are a good indicator of non-crystallinity. In $(H_2O)_{293}$, the smallest model with a crystal core, five-membered rings penetrate ~5 Å into the cluster. This result further supports adoption of 5 Å thickness for the surface layer of $n = 931$.)

Inspection of the $n = 931$ inner slice in figure 2 suggests that both the 'subsurface' and 'interior' components below the surface layer are quite well crystallized. One may then ask what is the source of broadening obtained in the subsurface spectra. The answer is apparent from table 1, which shows that the mean O···O hydrogen bond lengths, and the mean O···O···O angles between adjacent hydrogen bonds are quite similar for the subsurface and the interior molecules; however the corresponding standard deviations are significantly larger for the subsurface. The larger width of the distributions most likely reflects the strain induced by the interaction

of the subsurface with the disordered surface, and also by the residual presence of some five-membered rings within the subsurface (see figure 2, bottom panel, upper-right side). Elimination of the five-membered rings embedded in the subsurface and the inner surface is the likely slow activated relaxation process which leads to the conversion of the subsurface spectrum to the interior.

We then consider the dependence of the peak frequency of the bonded-OH band on the mean cluster size (figure 12). It is seen that just below the cluster diameter of 4 nm, the measured peak frequency increases from the crystal ice value of 3220 cm^{-1}, to ~3260 cm^{-1}; the latter value corresponds to the peak of the *surface* spectrum shown in figure 14. The peak frequency of the bonded-OH band then remains nearly constant down to the size of ~3 nm. One may recall that the measured spectra of ~3 nm particles include the same surface + subsurface components as the larger particles, but no 'interior' contribution (figure 4).

These findings can be understood in terms of the cluster structure, as follows. In the ~3–4 nm range, the majority of water molecules are within the *surface* layer. However molecular structure of this layer is still similar to that of larger crystalline nanoparticles; the surface structure appears to be dictated by the underlying core, which is still approximately crystalline. (The core of the small nanoparticles is significantly strained and therefore yields a 'subsurface' spectroscopic signature.) One may note in this context that the computed mean values and standard deviations of the O···O bond lengths and the O···O···O angles for the entire $(H_2O)_{293}$ cluster (diameter 2.7 nm) are similar to those of the *surface* of $(H_2O)_{931}$. The strained crystal core of $(H_2O)_{293}$ now contains only ~10% of water molecules (see figures 1 and 8, figure 12 of [23], and table 1).

For even smaller sizes, the particles 'run out' entirely of the crystal core. As seen in figure 8, the five- and four-membered rings (which are characteristic of non-crystalline material) now penetrate the entire volume of the cluster. The strain increases, as evidenced by the decrease in the mean value of the O···O···O angle from $n = 123$ to $n = 48$ (table 1). The increasing strain and the reduced volume of the amorphous core is reflected by the shift of the bonded-OH band to the blue, with the decreasing size (figure 12).

3.4. *Ice surface bending-mode spectra*

The spectra of the bending modes of the water molecules on the surface of ice particles have been investigated by combined FTIR and *ab initio* computations [125, 154] (figure 4). The intensity of the molecular bending mode of the core and subsurface ice is very low, so the bands for the bending modes of the three types of surface water molecules, d-H, d-O and s-4, stand out clearly. The argument was made that the bending modes of water molecules in the tetrahedral environments of the core and subsurface are vanishingly weak because of a combination of an inherently weak oscillator strength for the symmetric environments, and a mixing of the bend with the overtone of the librational mode. For the ice surface, the librational overtone is strongly redshifted and no longer suppresses the bending-mode bands. Consequently, a relatively sharp structured feature in the 1650 cm^{-1} range of the particle spectra has been attributed to the bending modes of surface molecules superimposed on the extremely broad librational overtone band of the interior molecules. The broad band can be removed, using the spectrum of large nanoparticles (60–80 nm) or thick ice films, leaving just the surface bending-mode bands (inset of figure 4).

Initially it was thought that the components for each category of surface-molecule bending-mode bands of figure 4 would have frequencies that increase in the sequence d-H, d-O and s-4, corresponding to increased bonding of the surface molecules. However, *ab initio* computations based on reduced-dimensionality models of the three categories of surface molecules indicate that (a) the s-4 frequency falls below that of the d-O but above that of the d-H molecules and (b) despite a greater population, the s-4 intensity contribution is quite low because of greater tetrahedrality [125]. It was concluded that, contrary to earlier reports [172], there is a strong but irregular dependence of the bend-mode frequency and band intensity on the H-bond strength and tetrahedrality of water structures. The variation of the computed surface bending oscillator strength across the band is indicated by the histogram at the bottom of the inset to figure 4.

3.5. *Interplay of ice-particle surface structure and adsorbate binding*

Ice particles are quite unique in possessing a number of 'localized' surface vibrational modes, d-H, d-O and s-4, with frequencies significantly different than the corresponding values of the particle core. (The notation s-4 pertains to 4-coordinated surface molecules with a coordination shell typically distorted from tetrahedrality.) The spectra of other particles, such as of CO_2 [123, 173, 174] and SO_2 [175], are characterized by intense bands of dipole-coupled oscillations with the normal mode frequencies significantly shifted by surface charges induced by the oscillations. However, such spectra are largely uninformative of surface properties at the molecular level, though there may have been a breakthrough in this respect in recent studies of CO_2 clusters [176].

In ice nanoparticles, several surface modes respond to adsorbates in unique and disparate ways that provide information about the bare surface, and the manner in which it adjusts to adsorbates. We have seen (Section 3.2.1) that SO_2 and other adsorbates of intermediate strength have the ability to de-reconstruct the ice surface through cleavage and insertion into weak surface H-bonds. In doing so, the experimental spectra confirm the predictions of simulations that the surface of an ice particle reconstructs at modest temperatures to sharply reduce the number of high energy reactive dangling bonds. This concept extends to the understanding of the interaction of the strong acids HCl and HBr (HX) with ice particle surfaces. There has been a considerable discussion in the literature, both experimental and theoretical, on the efficiency of acid ionization on flat ice surfaces [163–169]. Our experiments show that molecular (undissociated) HX is (kinetically) stabilized on the ice particle surface at temperatures < 90 K [177, 178]. MC and *ab initio* calculations indicate that the stabilization can be understood in terms of the reduced solvation of HX on a reconstructed ice surface deficient in d-H groups; so the HX molecular stability on the surface is itself informative of the ice surface structure.

Weak adsorbates, by contrast, do not disrupt the ice surface, at least of larger nanocrystals, but their presence is reflected by modest shifts in the positions of the modes of the surface water molecules. Such shifts are useful in pinpointing frequencies of the surface molecule vibrations [144]. Difference spectra of the coated versus the bare particles show pronounced minima at the bare ice values and maxima at shifted-band positions, as exemplified in figure 15 for the adsorbate benzene. Further, we have noted that one weak adsorbate, CF_4, is an excellent probe of the surface area of ice nanoparticles (Section 3.1.2; figure 9); but its usefulness goes beyond that of a probe of particle size. The CF_4 lineshapes as a function

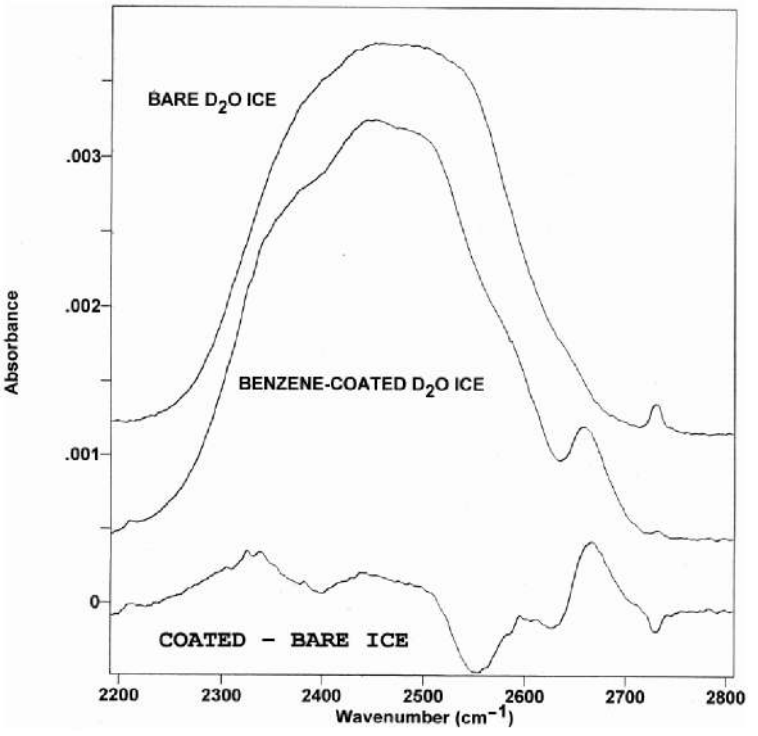

Figure 15. Comparison of the FTIR spectra of bare and benzene coated 2.3 nm amorphous ice particles. The spectrum shows the 8-fold enhancement of the intensity of the d-D band through interaction with the adsorbed benzene and the shifting of other surface subbands.

of coverage also provide a wealth of information on the extent of surface disorder and roughness, and on the sizes of water rings in the particle surface [18].

There is increasing evidence that even weak adsorbates can significantly influence local surface structure for the more flexible large water clusters. It has been known for several years, that in addition to modest shifting of surface-mode band positions of ice particles, weak adsorbates such as N_2 and CO significantly enhance the oscillator strength of the d-H mode [179]. This enhancement factor must be considered in viewing the spectra of N_2-covered water clusters (such as discussed in Section 4). Interestingly, more recent measurements have shown that the enhancement factor increases rapidly with decreasing particle size. The plots of figure 16 suggest a doubling of this factor for N_2 in the range 8–2.3 nm, while the factor more than triples for benzene over the same particle-size range. The origin of this increase is not known, but it likely includes structural changes induced in the mobile surface of the small non-crystalline strained clusters; including increased d-H populations from adsorbate insertion into the weakest surface H-bonds. Moreover adsorbate may reshape the small clusters towards optimization of bonding between adsorbate molecules and d-H, which would also affect the intensity. The strong influence of a benzene monolayer on ~2.5 nm particles is apparent from the comparison of the coated versus the bare spectra of figure 15, with the shift of the free-OD band from 2730 to 2670 cm^{-1} accompanied by an 8-fold increase in band intensity.

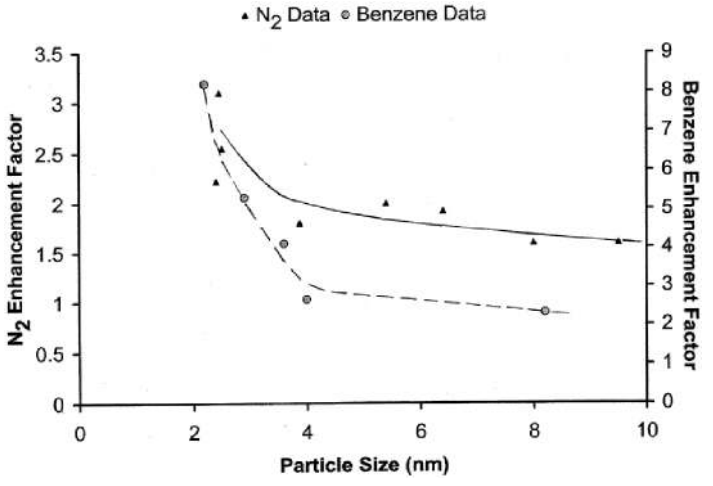

Figure 16. Variation of enhancement factors with particle size for several monolayers of the adsorbates N_2 (triangles) and benzene (circles). The factor is the ratio of the integrated intensity of the free-OH band for coated versus bare particles. The curves are only to aid viewing the dependences.

4. FTIR approach to the 1–5 nm diameter range of ice particles (~20–2000 molecules)

Extending the studies of Section 3 we describe here first results gained from FTIR spectra of smaller ice particles generated in a long-path collisional cooling cell between 4.5 and 78 K. While the adiabatic jet expansion techniques are well suited to produce size-selected smaller clusters (2–12 molecules per particle), larger clusters (~200–10^9 molecules per particle) can be favourably investigated with the collisional cooling techniques (see Section 3 and [22]). However, the interesting surface-dominated size region of about 10 to 300 molecules per particle remained not satisfyingly accessible to either method. Therefore, a collisional cooling approach coming from the high side of the particle size range and working in thermal equilibrium seemed promising. In the meantime, a completely different cluster-surface sensitive access to this size range (based on photofragment spectroscopy and adiabatic jet expansion) has been developed as well, see Section 5.

As mentioned above, two factors are crucial for the generation of small nanoparticles by collisional cooling: (a) high nucleation rate caused by high supersaturation of the water vapour in the carrier gas which can be managed by rapid cooling, with a cooling rate as high as possible; (b) low water vapour density which ensures a limited growth of the nuclei. Stable small ice particles in thermal equilibrium are possible at lower temperatures because the size of the critical nucleus decreases with temperature (Dillmann–Meier and Becker–Döring theory [181–183]), and is smaller than 20 water molecules for temperatures below 200 K (~10 water molecules below 100 K [184]).

4.1. *Liquid-helium temperature long-path collisional cooling technique*

To achieve these preconditions, the cooling system was designed for liquid helium operation to realize high cooling rates [123]. An integrated White optics system proved to be necessary to ensure the sensitivity needed for the relatively small water concentrations of about 1 ppm H_2O in He. Additionally, a (multi)pulse-inlet system

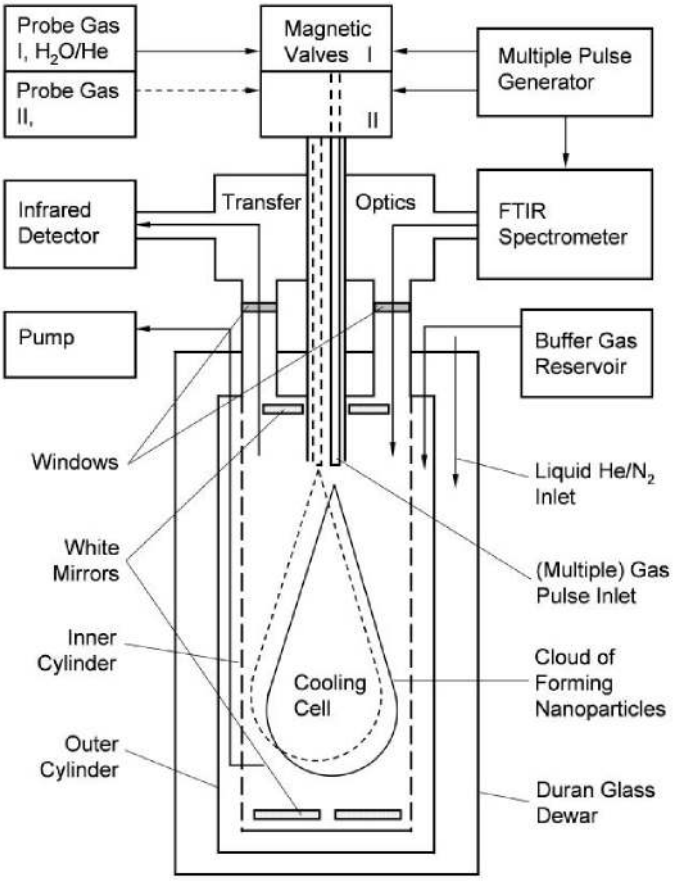

Figure 17. Schematic view of the experimental set-up for FTIR spectroscopy of particles in a long-path collisional cooling cell, discussed in Section 4. The present cooling method combines (1) liquid-helium cooling, (2) optical path-length of up to 20 m (FTIR operation) or up to 40 m (laser operation), (3) electric heating system (not shown here) consisting of a three-zone heating around the inner cylinder, mirror heating and sample-gas inlet heating which enable work at temperatures in the range of 4.2–400 K, (4) vertical cell arrangement that allows us to keep mirrors and seals at room temperature, and (5) a sample-gas inlet system for pulsed operation to investigate multicomponent aerosols.

has been developed for rapid pulse-injection of the sample gas within 60 ms into the precooled buffer-gas in the cell to enhance the supersaturation.

The experimental set-up is shown in figure 17. Apart from one, all the gaskets for windows, inlet and outlet tubes, etc., and the windows themselves are kept at room temperature during operation. In that way, as an advantage of the vertical cell arrangement, neither leak problems nor deposits on the windows from inside or outside occur. The whole cell is immersed in liquid or gaseous helium or nitrogen as coolants. The FTIR or laser beam is inserted into the cell and guided to an infrared detector via transfer optics. Maximum optical path-length is 20 m for FTIR and 40 m for laser operation. Temperatures range from 4.2 to 400 K; the buffer gas pressure can be held between 10^{-3} mbar and a few bar; particles in the mean size range of $n < 20$ to $n > 10^{14}$ can be investigated.

For particle generation the cooling cell is first filled with He or another inert gas which adapts to the adjusted operation temperature. Then the sample gas mixture is rapidly injected out of a variable-volume reservoir at a pressure in the range of 0.1 to 5 bar into the cold buffer gas. For that purpose electromagnetic valves are used. The pulse length and pause length between two successive pulses can be adjusted from 60 ms to continuous flow. The maximum repetition frequency is about 4 per second. The sample gas typically cools down to the buffer gas temperature within 100 ms. During this period nucleation and particle growth take place and an aerosol cloud forms which immediately occupies the volume. Then it can be spectroscopically observed in thermal equilibrium over minutes to hours. In general, particles are lost by diffusion into the space between the inner and outer cylinder, sedimentation, Ostwald ripening at higher temperatures, or other processes.

The sample gas inlet system is constructed for multiple injection of different gases, see dotted lines in figure 17. This multipulse injection technique allows studying the interaction of aerosol/monomer clouds of different molecules during combined or successive nucleation and particle growth. For example, nanoparticles composed of a core with a mantle of different kinds of isotopes ($^{12}CO_2/^{13}CO_2$) [185] or of different kinds of molecules (CO_2/H_2O) [186] can be investigated. The whole cooling technique is described in detail in [123].

4.2. *Experimental conditions*

The spectra presented in figure 5 were obtained with the following experimental parameters. The most important are the water concentration of the sample gas and the buffer-gas temperature, which range from 1 to 100 ppm H_2O in He and from 4.5 to 78 K (see legend of figure 18). The buffer gas pressure, which is less important for the particle size, varied between 40 to 200 mbar. Recording of the spectra started 3 s after sample gas injection. The measuring time was 159 s (except for 30 s each for spectra 6 and 7). The optical path-length was 15 m, and the spectral resolution was

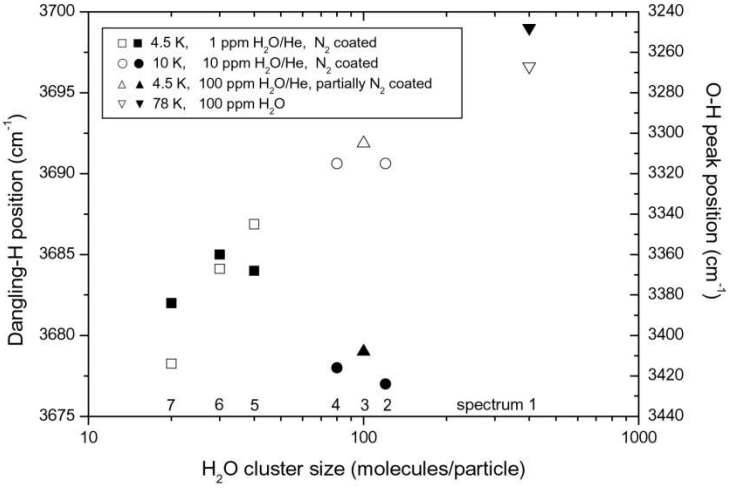

Figure 18. Variation of peak positions of the free-OH band (filled symbols) and of the bonded OH band (unfilled symbols) with the cluster average size, related to the spectra shown in figure 5. Note that spectra 2–7 are redshifted by about 20–25 cm^{-1} due to N_2 coating of the clusters. The inset assigns the most important experimental parameters determining the cluster size.

$4\,cm^{-1}$ (apart from $8\,cm^{-1}$ each for spectra 6 and 7). A typical half-life of the smaller particles within the optical beam volume is about 500 s in the temperature range of 4.5 to 10 K.

In contrast to the experiments of Section 3 for which no precooled buffer gas was introduced, and higher cell temperatures were employed, we here assume that Ostwald ripening can be neglected (especially for the measurements between 4.5 and 10 K, as in spectra 2–7 in figure 5). The reason is that the vapour pressure of water ice decreases drastically with the temperature in this range (below 10^{-22} mbar for 78 K and below 10^{-117} mbar for 20 K, see the Goff–Gratch equation and [188]). The vapour pressure enhancement for small particles due to the Kelvin effect does not decisively change the situation, once particles are cooled below ~100 K [153].

At favourable conditions for the generation of small ice particles (see spectra 5–7 in figure 5), that is low concentration and temperature, the nucleation rates indicated by the formation of $n \sim 10$ clusters can be estimated at 10^{16}–$10^{19}\,cm^{-1}\,s^{-1}$. This assumes 10^{18}–10^{20} molecules per pulse, a nucleation volume of $1000\,cm^3$ and a nucleation time of 10–100 ms. These nucleation rates are about 7–10 orders of magnitude higher than those determined in experiments using adiabatic expansion chambers at higher temperature [184, 187].

4.3. *Cluster size estimation; comparison of measured and calculated spectra*

The spectra shown in figure 5 are assigned to smaller clusters, with decreasing size from top to bottom as in figures 3 and 4. It is remarkable that spectrum 1 (top) matches exactly the bottom 2.8 nm spectrum of figure 4 in peak positions, band shapes and integrated band absorbance, and therefore represents the link between the two series of FTIR spectra. Comparing the most important parameters of the underlying experiments of both spectra, that are mainly temperature and sample-gas water concentration, it turns out that the lower temperature in one experiment is compensated by a lower water concentration in the other, resulting finally in similar cluster sizes. From the comparison of the two sets of spectra and considering the information of figures 11 and 12, we determine the average size of the biggest particles in the series of spectra (spectrum 1 of figure 5) to be $n \sim 400$ molecules. In general, we assume that the size distribution of nanoparticles generated by collisional cooling to be a log-normal one [153, 189].

Estimation of the mean size of the smaller particles is more problematic. The $\sim 20\,cm^{-1}$ redshift of the free-OH band indicates that clusters contributing to spectra 2–7 are covered by adsorbed N_2 contaminant (see also figure 18). Spectrum 1, measured at 78 K, is the only one that shows no redshift of the d-H peak position; the N_2 molecules, if present, do not seem to adsorb on the ice surface at this temperature. Due to the low H_2O concentrations and low temperatures (4.5–12 K) needed for smaller particles, small amounts of N_2 in the sample gas have a noticeable impact.

The decreasing integrated intensity ratio R between the bonded-OH band and the free-OH band is consistent with a decreasing mean cluster size in the sequence of spectra 2, 4–7. However, in contrast to the bare cluster case, the ratio cannot be used for quantitative estimation of the average n value, because of the size-dependent intensity enhancement factor of the free-OH band by the adsorbate (see Section 3.5 and figure 16). Spectrum 3 appears to be out of sequence, since the R-value is larger than in spectrum 2. However the higher frequency of the bonded-OH peak indicates

smaller rather than larger average cluster size. This observation can be accounted for by the relatively large width of the free-OH band in spectrum 3, which points towards *partial* N_2 cluster surface coverage; resulting in reduced integrated intensity of the free-OH band.

The peak frequency of the *bonded*-OH band still appears to be a valid qualitative probe of the cluster size. This is because spectra of N_2-covered larger particles (as examined for purposes of figure 16) showed that N_2 adsorbate has a weak (though noticeable) effect on the position of the bonded-OH band. The sequence of spectra 1–7 displays gradual shift of the bonded-OH band to the blue (see also figure 18), in accord with the computed trends for clusters with decreasing size (figure 3). The bottom experimental spectra appear similar to the ones computed for $n = 48$ and $n \sim 20$, respectively. Based on the similarity, we tentatively assign spectra 5–7 to clusters of average size of a few tens of molecules ($\sim$1 nm diameter, $n \leq 50$).

As noted in Section 2.3.2, clusters with a few tens of molecules are characterized by a strained hydrogen-bond network, in which about half of H_2O are 3-coordinated. From comparison of spectra 5–7 to calculations (figures 3 and 7), the feature above 3500 cm^{-1} is assigned to d-O molecules, the centre peak is dominated by 4-coordinated H_2O with a strained coordination shell, and the low frequency feature at 3213cm^{-1} originates from 'companion' bonded-OH of d-H molecules.

Two main discrepancies are apparent between the experimental spectra 5–7, and the two bottom calculated spectra of figure 3. First, the computed 'companion' feature appears below 3100 cm^{-1}, while the experimental one appears just above $\sim$3200 cm^{-1}. This discrepancy seems to be due to the inaccuracy of the computational model. An analogous feature is seen more clearly in the photofragment spectra discussed in the next section. There, the spectra are dominated by 3-coordinated surface molecules; and a similar deviation is obtained with respect to computed low frequency peak of the surface spectrum.

The second difference between the measured spectra 5–7 and their computed counterparts is a much lower relative intensity of the free-OH feature in the latter. Even N_2 adsorbate enhancement of the computed free-OH band by a factor of 3 (as measured for $n \sim 200$ particles, see Section 3.5) does not alleviate the discrepancy. The measured R values in spectra 5, 6 and 7 are 26, 18 and 11, respectively, while the computed values for $n = 48$ and $\sim$20 are 230 and 160. The comparison suggests a remarkably large enhancement factor of the free-OH intensity by about an order of magnitude, due to the presence of N_2 adsorbate on the small clusters. Figure 16 is in fact consistent with sharp increase in the enhancement factor with decreasing size.

An additional contribution to the small measured R value may originate from intrinsic intensity enhancement of the free-OH feature in the strained small clusters, as compared to the larger ones. One may note in this context the remarkably large free-OH intensity measured in the past for $n \leq 10$, by a variety of techniques [112, 113, 104]. One may also note, that the detailed dependence of the bond dipole derivative on the H_2O bonding configuration is not known, which limits the accuracy of the calculation. (The present model employs a simple extrapolation scheme between gaseous H_2O and ice; see Section 2.3.)

Based on spectra 5–7, the last point of figure 12 was set at 1 nm, with centre frequency at 3370 cm^{-1}. Spectra 2–4 correspond to peak frequencies in the 3305–3345 cm^{-1} range. Interpolation of figure 12 suggests cluster diameters of $\sim$2 nm, or $n \sim 100$ molecules. At this size, the clusters are fully amorphous (Section 2).

The experimental R values for spectra 2 and 4 are 75 and 46, respectively, while the R value calculated for (bare) $n = 123$ is 310, suggesting an enhancement factor of ~6 of the free-OH band due to N_2 adsorbate. It is notable that for spectra 2, 4–6 (originating from fully coated clusters), the free-OH frequency increases with decreasing size, while for the smallest size (spectrum 7), a decrease in frequency is observed (see also figure 18); the decrease could be due to particularly strong interaction of free-OH with adsorbate, offsetting the effect of increasing strain.

One may wonder finally whether the smallest observed particles of spectrum 7 could correspond to even smaller sizes than estimated above, such as $n \leq 10$. The size-selected spectra for $n = 7$–10, measured in the past by Buck *et al.* [104, 105] appear to contradict this suggestion, since the measured spectra for $n = 8$–10 included a prominent 'companion' peak at ~3100 cm^{-1}, which in spectrum 7 appears at a significantly higher frequency. However the spectra of [104, 105] pertain to bare clusters. The small clusters are fairly flexible, and have numerous low energy minima. The ones with favourable binding sites with respect to N_2 adsorbate may have significantly different structures than the bare ones. (The presence of such favourable sites is indicated by the large free-OH intensity enhancement by adsorbate.) Computations indicate, for example, that the sequence of energies of isomers of small water clusters on a graphite surface differs from that of the bare clusters [190]. Thus it is conceivable that clusters contributing to spectrum 7 correspond to $n \leq 10$, with structures and spectra modified by N_2.

In summary, it was shown that the transition to smaller particles from one experimental collisional cooling technique (Section 3) to another presented here is smooth, in spite of the different approaches to cooling of sample gas mixtures. Spectroscopic data were extended to include cluster sizes of tens of H_2O. Reasonable qualitative correspondence was observed between the measured and computed trends with decreasing size. Presence of N_2 adsorbate complicates somewhat the interpretation of the experimental results. Future operation with less N_2 impurities appears to be possible [191].

5. Photofragment spectroscopy of water clusters with mean size of 20–2000 molecules

In the present contribution we address clusters which are generated in a different way than in Sections 3 and 4, and we also apply a different spectroscopic technique using two novel approaches which allow us (i) to work with known average sizes and (ii) to apply IR spectroscopy which proved to be mainly sensitive to the outer surface of these clusters. The size range is at the lower end of the previously described experiments in the range between the lower tens to several thousands. The clusters are produced by adiabatic expansions through nozzles of small diameter in molecular beams free of interaction. The sizes are determined by doping the clusters with single Na atoms which are detected nearly fragmentation-free by photoionization close to the threshold [26]. We shall present a correlation that relates the water cluster sizes to the source conditions of the adiabatic expansion. For the IR-spectroscopy of the OH stretch mode we have chosen the fragment spectroscopy, since the well established depletion technique which was successfully used in the spectroscopy of completely size-selected small water clusters [104, 105, 192] is not very sensitive to the small change in the total mass which we have to anticipate for large clusters. The fragment spectroscopy for water clusters was used previously by detecting H_3O^+ but without accurately knowing the size [193, 194]. Here, we were

able to extend these measurements to larger units up to $(H_2O)_4H^+$ which proved to be sensitive to the cluster surface. Results will be presented mainly for the average cluster sizes $\langle n \rangle = 40$, 111, 631, and 1960. They will be compared with calculated spectra which have been obtained from low energy structures for $n = 48$, 123, 600 and 931 [23, 25]. In this way we shall be able to compare the results of the previous sections with the results obtained here by a different experimental approach concerning both the generation of the clusters and thus their sizes, and the spectroscopic method as well.

We shall start this part with a brief description of the experimental set-up and how the cluster sizes are determined. Then we shall discuss the dissociation process with the help of the measured angular and size dependence of the different fragments and their sensitivity to the location within the structure of the clusters. The direct comparison with the calculated IR spectra reveals that our measurements are neither reproduced by the spectra of the complete clusters nor by that of their surfaces which were deduced for the ice nanoparticles as described in Section 3. Rather, our new measurements are mainly sensitive to the *outermost* surface of the clusters. This part of the clusters was argued to be always disordered in the size range investigated here. In addition, the size dependence of the fragment signal exhibited an indirect sensitivity to size and structure of the core of the larger clusters.

5.1. *Experimental methods*

5.1.1. *Overview*

The experiments have been carried out in a molecular beam machine which has been described in detail previously [195, 196]. The large water clusters are produced in a supersonic expansion of mixed and pure water vapour at 2–22 bar through nozzles of conical shape with diameters between 50 and 90 μm, opening angles between 20° and 41°, and 2–6 mm length. The average size of the resulting cluster distribution is determined by applying the recently developed method of doping the cluster by pick-up of Na atoms [26] which is described in detail in the next section. The vibrational spectra of the pure large water clusters $(H_2O)_n$ are measured in the schematic experimental arrangement depicted in figure 19. The pulsed, tunable infrared radiation crosses the cluster beam in a quasi-collinear configuration under a small angle and is tuned in a frequency range from 2800 to 3800 cm^{-1}. It is obtained from the Nd:YAG-laser-pumped optical parametric oscillator (OPO) [197]. It consists of a $LiNbO_3$ crystal with a typical output of the laser fluence from 100 to 500 mJ/cm^2 per pulse and a bandwidth of 0.2 cm^{-1}. We note that, because of a water impurity of the crystal around 3500 cm^{-1}, an intensity gap arises in this frequency region.

If a vibrational mode of the clusters is excited, the energy is redistributed and leads to the decay of the cluster. For small water clusters this decay is usually detected by the depletion of the signal [104, 192]. This method is not very suitable for large clusters, since the change in the signal is quite small. Here the detection of the

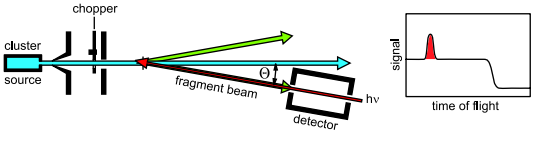

Figure 19. Schematic view of the experimental set-up for measuring photofragment spectra.

fragments is much more appropriate. Therefore the detector, a rotatable quadrupole mass filter with a continuous electron bombardment ion source, is positioned at an angle Θ of about 2.0–4.5° with respect to the water cluster beam. A chopper allows digital lock-in (DLI) measurements, to discriminate the signal of the continuous water cluster beam from background. Neutral fragments leave the clusters as a result of the excitation and diverge from the water cluster beam. Therefore they are detected as enhancement of the signal following the laser pulse in the time-resolved ion signal of the tuned masses.

5.1.2. *Cluster sizes*

The average size of the cluster distribution is determined by applying the recently developed method of doping the cluster by the pick-up of Na atoms [26]. In this way the cluster can be ionized free of fragmentation by single photons close to the threshold, since the ionization potential is significantly reduced to 3.2 eV. In the present experiment the photoionization takes place by a dye laser operated at the wavelength of 360 nm (3.46 eV). Typical size distributions are shown in figure 20 for $\langle n \rangle = 631$ and 1721, where the clusters were generated under the following experimental conditions. The gas expands through a nozzle of conical shape with a diameter of 50 µm, an opening angle of 41°, and a length of 2 mm at a temperature of 495 K. By varying the pressure from 11.0 bar to 19.6 bar the two different size distributions are obtained. The solid line is a fit to the experimental data using the log-normal distribution

$$f(n) = \frac{1}{\sqrt{2\pi}\sigma n} \exp\left[-\frac{(\ln n - \mu)^2}{2\sigma^2}\right] \tag{1}$$

with the two parameters μ, the logarithm of the geometric mean, and σ, the logarithm of the geometric standard deviation. The mean cluster sizes $\langle n \rangle = 631$ and 1721 which are also marked in the figure are directly determined from the fit. This example clearly shows that, in spite of the relatively large width of the distributions, a completely different size range is probed in the two experiments.

Based on a series of such results we have derived a scaling law [26] which relates the mean cluster size $\langle n \rangle$ with the source conditions of the expansion, in the spirit

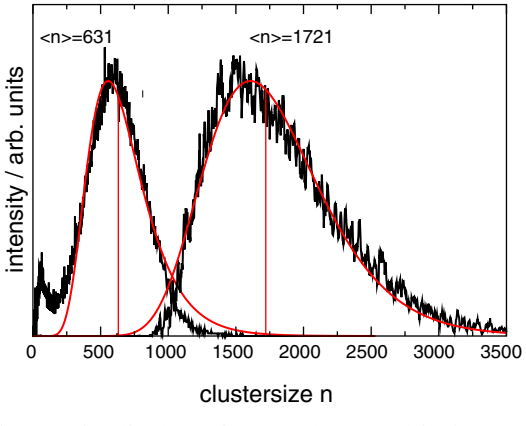

Figure 20. Measured mass distribution of water clusters with the mean size $\langle n \rangle = 631$ and 1721 indicated by the vertical lines. The solid line is a log-normal distribution fitted to the measurement.

of the well known scaling laws derived by Hagena for rare gases and metals [198, 199]. The key parameter that correlates the flow which produces the same cluster size is given by

$$\Gamma = n_0 d^{\,q} T_0^{\alpha} \quad (0 < q \leq 1). \tag{2}$$

Here n_0, T_0, and d are the source density, nozzle temperature and nozzle diameter. For nozzles with a conical shape and an opening angle of 2β, d has to be replaced by $d_{\mathrm{eff}} = 0.933/\tan\beta$ where the number is valid for polyatomic molecular systems. It is convenient to reduce the length and energy scales by the reduced parameter $\Gamma^* = \Gamma/(r_{\mathrm{ch}}^{q-3} T_{\mathrm{ch}}^{\alpha})$ with the characteristic values $r_{\mathrm{ch}} = 3.19\,\text{Å}$ and $T_{\mathrm{ch}} = 5684\,\mathrm{K}$ which are calculated from the density and the sublimation enthalpy of water. Then we are able to present the relation of the average cluster size $\langle n \rangle$ with the reduced source parameter Γ^* by a simple power law:

$$\langle n \rangle = D\left(\frac{\Gamma^*}{1000}\right)^{a}. \tag{3}$$

Thus in a log-log plot of the size $\langle n \rangle$ and the reduced parameter Γ^* a linear behaviour should result. This is demonstrated in figure 21. The solid line through our data which are represented by black points corresponds to the parameters $q = 0.643$ and $\alpha = -2.655$ of equation (2) and $D = 2.63$ and $a = 1.872$ from equation (3). *In this way the sizes of water clusters generated in adiabatic nozzle expansions are calculated from the source parameters*. These results fit very well the reported sizes of other groups which are also depicted in figure 21. The results of an electron diffraction experiment [5, 6] and two mass spectrometer studies [200, 201] follow nicely our data curves. We conclude that simple scaling laws of the type of equations (2) and (3) are also valid for water clusters.

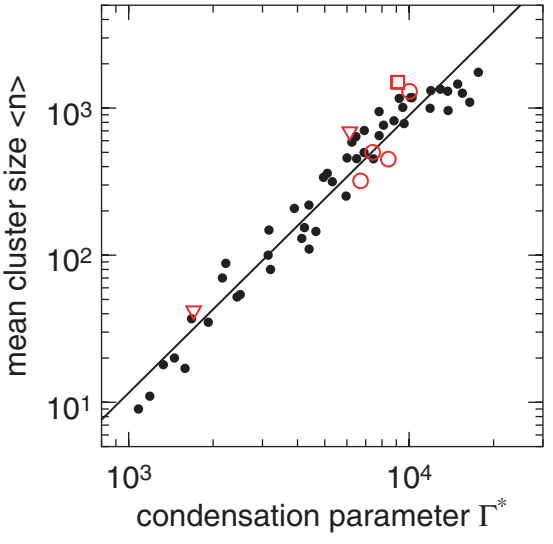

Figure 21. Mean cluster size as a function of the reduced scaling parameter for water clusters. Closed points: this work; open circles: [200]; triangles: [201]; squares: [5, 6].

5.2. *Photofragment spectroscopy*

The pulsed infrared radiation excites the OH stretch vibrational modes of the water clusters and the resulting predissociation is detected by the outgoing fragments. A typical angular distribution of the fragments is shown in the left hand panel of figure 22. The mean cluster size of the water cluster beam was $\langle n \rangle = 300$, and the excitation occurred at $3718\,\mathrm{cm}^{-1}$, the position of the free OH stretch motion of the water clusters. The rapid fall off from a peak at 0° is an indication of very small translational energy and large internal excitation. As expected from the kinematics of a direct reaction, the smaller fragments are scattered into larger angles as is manifested in the flatter slope. The most remarkable result, however, is the high intensity of the heavier fragments $(H_2O)_kH^+$ with $k = 2$–4 with respect to H_3O^+ with $k = 1$. This is displayed in the right hand panel of figure 22 for a fixed angle. The species with the largest intensity is that with $k = 4$. At both ends of the investigated fragment masses the intensity is smaller. If we take into account the well known fragmentation [202] of the water clusters by electron impact ionization, where in addition to the protonation at least one monomer is lost for complexes larger than the dimer, we have the surprising result that fragments of the neutral precursor hexamer, and to a lesser extent also those of the pentamer and tetramer, are much more frequent than those of the dimer. This is in contrast to measurements of pure [193] and methanol doped [194] water clusters with sizes smaller than $\langle n \rangle = 20$, which yielded the largest intensities for the smallest fragments. In fact, in molecular dynamics simulations where large water clusters were excited by raising the temperature, we found exactly the latter result [25]. Thus the result of our experiment is not what one would expect when energy is statistically distributed over the cluster. Apparently, a dissociation mechanism other than evaporation resulting from heating of all degrees of freedom is operating under the conditions of our experiment.

In the vibrational predissociation of binary complexes the coupling of the vibrational motion with free translational motion in the dissociation continuum leads to the momentum gap law which states that the translational motion of the product is minimized at the expense of the excitation of the next lying internal state [203–205]. In a system with many more internal degrees of freedom like in large

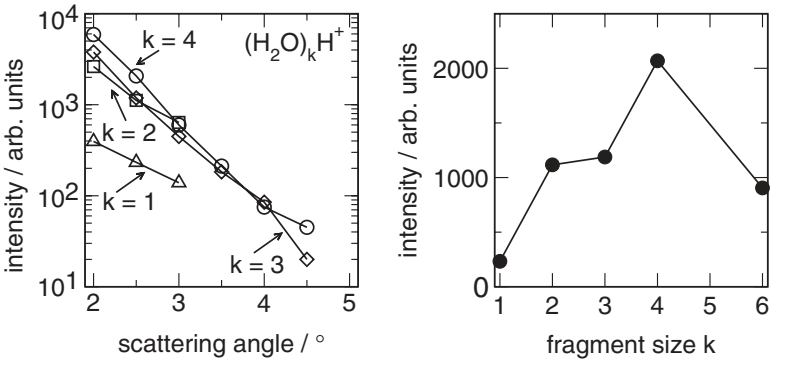

Figure 22. Left panel: measured angular dependence of the indicated ion signals $(H_2O)_kH^+$ at the mean cluster size of $\langle n \rangle = 300$ and a wavelength of $3718\,\mathrm{cm}^{-1}$ (free OH). Right panel: measured fragment size dependence of the $(H_2O)_kH^+$ ion signal at the detection angle of 2.5°. The corresponding parent clusters usually have larger masses because of fragmentation in the ion source.

water clusters the lifetime of the system is composed of two contributions [193]:

(i) The energy transfer from the initially excited *intramolecular* modes into the intermolecular cluster modes; here the coupling between these two groups of states plays a crucial role.

(ii) The next step is then the decay of the excited cluster along the *intermolecular* coordinates and the subsequent ejection of the photoproducts. The latter is likely to be in competition with energy redistribution throughout the cluster.

A further complication arises from the fact that at least two photons are necessary for the dissociation as will be discussed later in Section 5.4. This will usually affect the intensity and the width of the peaks in the spectrum. The analysis of the photodissociation spectra of clusters of a series of hydrogen bonded systems, however, showed that the fluence dependence is linear [206]. The reason is that the decay rate from the final state and thus the linewidth is large so that it can be reached in two subsequent one-photon transitions. In addition, the general width of the dissociation spectra is dominated by inhomogeneous broadening due to internal excitation effects.

To get more experimental information on the problem of the decay rates, we have measured the dependence of two characteristic fragment signals $(H_2O)_4H^+$ and H_3O^+ on the cluster size. The size variation is achieved by changing the pressure in the range from 1.5 to 21.5 bar at constant nozzle temperature of 495 K. The experiments are carried out for two different wavelengths, 3718 cm^{-1} and 3200 cm^{-1}, which correspond to the free and hydrogen bonded OH stretch modes. The results are presented in figure 23. In addition to the variables already discussed, the measurements were conducted for two different cluster temperatures. This was obtained by using two different lengths of the conical shaped nozzle under otherwise similar conditions. The longer conical nozzle of 6 mm (50 μm diameter and 41° opening angle) leads to a substantially longer interaction time compared to the 2 mm nozzle (60 μm diameter and 20.4° opening angle) before the zone free of interaction is reached. Therefore the cooling by collisions with the remaining monomers is more effective and we estimate a colder cluster temperature in this case. Therefore the results obtained with the different nozzles are marked with *warm* in the upper panel and *cold* in the lower panel.

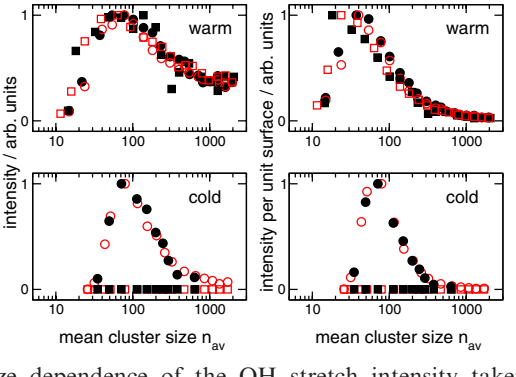

Figure 23. Cluster size dependence of the OH stretch intensity taken at 3718 cm^{-1} (full characters) and 3200 cm^{-1} (open characters) at the mass $(H_2O)_4H^+$ (circles) and $(H_2O)H^+$ (squares) for different temperatures. Right panels: the signal was renormalized per unit cluster surface.

Let us summarize the results presented in the left panels of figure 23, which show the fragment intensity as a function of $\langle n \rangle$. (1) There is, in general, no difference in the results for the two laser excitation energies. (2) We observe a pronounced size dependence of the $(H_2O)_4H^+$ signal for cold clusters. The distribution rises from $\langle n \rangle = 30$ to a peak at about $\langle n \rangle = 70$, and falls off to about $\langle n \rangle = 300$ where a tail begins which goes to zero for very large cluster sizes. (3) In the case of the warm clusters, the distribution is broader, the maximum is the same, and the tail exhibits higher intensities. (4) The H_3O^+ signal is zero for the cold cluster temperature. For the warm cluster the signal follows, with some deviations, the general trend of the heavier fragment; at small sizes before the maximum the dimer intensity is larger than the hexamer intensity. The right panels show the fragment intensity estimated *per unit cluster surface*; this presentation is of interest since, as argued in more detail below, fragment ejection appears to be a surface process. In this presentation, the intensity is similarly peaked at the size of several tens of molecules, but the tail at large $\langle n \rangle$ is reduced substantially.

We then measured the vibrational predissociation spectra in the full wave number range of 3000–3800 cm^{-1} which covers the complete OH stretch excitation. The average cluster sizes which are determined from the source parameters [26] as was described in Section 5.1.2 include $\langle n \rangle = 40$, 111, 631, and 1960. The two largest clusters were produced by the expansion of pure water vapour through a conical nozzle of 50 μm diameter, 2 mm length, and an opening angle of 41° at a nozzle temperature of 495 K and the pressure of 11 or 21 bar, respectively. The corresponding data for the two smaller clusters are a conical nozzle of 60(90) μm diameter, 6(2) mm length, and an opening angle of 20.4° (30°) at a nozzle temperature of 495(355) K and water vapour pressure of 3.0 (2.3) bar (16.7% water in helium) for $\langle n \rangle = 111(40)$. The spectroscopic data were, in general, taken at the mass of the fragment ions $(H_2O)_4H^+$, that are attributed to the parent neutral water hexamers $(H_2O)_6$. In the case of the largest cluster $\langle n \rangle = 1960$, we also detected the $(H_3O)^+$ fragment which is attributed to the dimer. The spectra for the two smaller sizes are taken in the configuration which produces cold clusters, while those of the larger size are generated with warm clusters. This definitely follows from the results obtained in figure 23. The experimental results of these OH-stretch spectra are depicted in figure 6. The gap around 3500 cm^{-1} is the artifact of the experimental arrangement already mentioned in the experimental section. The spectra are dominated by peaks at 3720 cm^{-1} and 3550 cm^{-1} for all sizes, and a variable peak for the smaller clusters moving from 3420 cm^{-1} to 3350 cm^{-1} (marked by the straight line). Peaks in this range continue to be present also for the larger clusters. The larger clusters exhibit, in addition, a peak with increasing intensity near 3220 cm^{-1} which is not present for the smaller clusters. The latter exhibit, in contrast, a peak below 3200 cm^{-1}.

5.3. *Comparison of measured and calculated spectra*

We note that the amplitudes in these measurements do not reflect the IR absorption cross-sections, but are the product of these with the coupling of the respective intramolecular motions to intermolecular excitation along the H bonds leading to the dissociation of the clusters [206]. The comparison of the experimental photofragment spectra in figure 6 and the calculated absorption spectra for the entire cluster, in figure 3 shows that, for $\langle n \rangle = 40$ and 111, at least the trend, indicated by the straight line, is reproduced. It is caused by the decreasing number of amorphous 4-coordinated surface molecules. A closer look, however, reveals that

there is qualitative disagreement in the intensities, while the calculations are in good agreement with the the experimental FTIR spectra obtained in a cold condensation cell (figures 4 and 5). The discrepancy is especially striking for the larger cluster sizes, for which the calculated bonded-OH band (for the entire cluster) peaks at $\sim$3200 cm^{-1}, while the experimental one (in photofragment spectra) extends, with relatively modest variation of intensity, from $\sim$3100 to 3550 cm^{-1}. On the other hand, much better agreement can be expected while comparing the predissociation spectra with the computed *surface* spectra of the example in figure 14; there, the maximum shifts to larger wave numbers, but the spectrum still does not correspond to fairly uniformly distributed intensity over the whole measured frequency range.

In Section 3, the relatively large cluster surface thickness of about 0.5 nm was derived using enhanced relaxation rate as a criterion. It appears that photofragment spectroscopy probes a significantly thinner outer-surface layer, with fewer 4-coordinated molecules. Apparently, only absorption events by *outer* surface molecules lead to formation of photofragments. Thus, calculations are brought into qualitative agreement with the photofragment spectra by including only absorption intensity by molecules, whose distance from the cluster centre-of-mass exceeds some cutoff radius r_c. The computed distribution of molecules of different coordinations as a function of distance from the cluster centre-of-mass is shown in figure 24. To match the experimental spectra, r_c values were adopted at a distance at which 3-coordinated molecules start to dominate the distribution. These values are marked by arrows and correspond to a point at which the solid line crosses the dot-dashed line (i.e., at 5 Å for $n = 48$, and 18 Å for $n = 931$). The resulting spectra are depicted in figure 6. Based on these cut-off radii we obtain indeed a fairly uniform intensity distribution over the entire bonded-OH range.

The final step is now the comparison with the measured data, shown also in figure 6. For $\langle n \rangle = 40(48), 111(123)$ and 631(600), cluster models of similar size

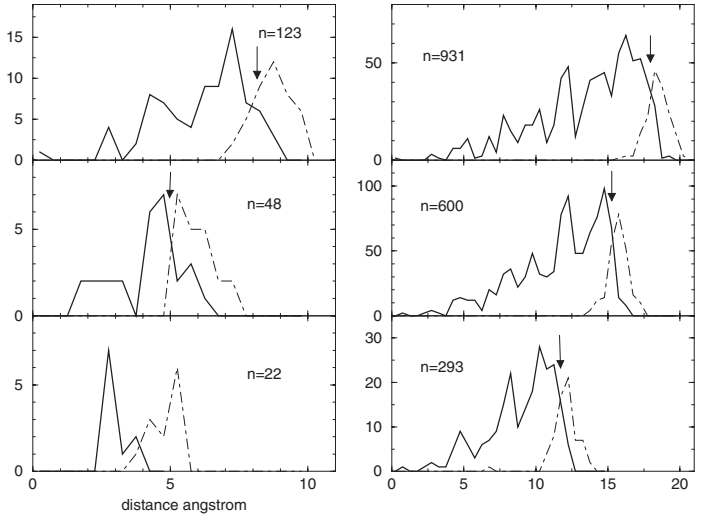

Figure 24. Distribution of molecular distances from cluster centres-of-mass, for lowest energy structures found. Solid line: 4- and 5-coordinated molecules (predominantly 4-coordinated); dot-dashed line: lower coordination (predominantly 3-coordinated). The arrow denotes cutoff for the definition of the surface layer, used in the calculation of surface spectra in figure 6.

(in parentheses) are available. The data for $\langle n \rangle = 1960$ had to be compared with the calculations for $n = 931$ which is the largest size treated theoretically up to now. This difference, however, does not appear to be very important since in the $n \sim 1000$–2000 range the cluster structure is composed of similar elements (crystal core, subsurface, disordered surface; see Sections 2 and 3). The only adjustment which has been made in this comparison is to shift the complete spectrum by $32\,\mathrm{cm}^{-1}$ so that the position of the free-OH is matched. The over-all agreement between experiment and calculations is remarkable. Deviations occur in the intensity of the peaks for the free-OH stretch mode, these deviations are discussed in more detail in the next section. There are also small shifts in the positions around $3550\,\mathrm{cm}^{-1}$ and pronounced peaks appear in the calculation below $3100\,\mathrm{cm}^{-1}$.

To improve the agreement with the two top experimental spectra in figure 6, we have compared the results with computed spectra corresponding to different cutoff distances. The direct comparison is presented in figure 25. The dimer spectrum matches better the calculation for $r_c = 18.5\,\text{Å}$, while the hexamer spectrum agrees better with $r_c = 17.5\,\text{Å}$. This suggests that the dimers emerge from the very top of the surface layer, while the excitation depth for producing the hexamers is somewhat larger. Dimers are more difficult to produce (since they are obtained only from warm clusters), and they come, if at all, from the outmost surface layer.

We are now able to assign the peaks in the experimental spectra based on the decomposition of the computed spectra to contributions from different coordinations (see figures 7 and 25). In accord with past studies [104, 144], the free-OH of DAA (d-H) molecules give rise to the narrow highest frequency band, while the bonded-OH of the DAA molecules dominates the low frequency end of the spectrum. At $\langle n \rangle \sim 40$, DAA molecules give rise to a prominent, separate band at the low frequency end of the spectrum both in experiment and in calculation,

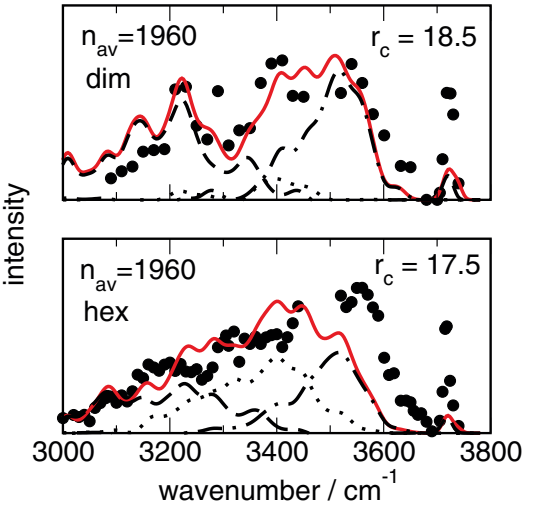

Figure 25. Comparison of the calculated surface spectra (solid lines) for $n = 931$ with two different cutoffs $r_c = 18.5\,\text{Å}$ and $r_c = 17.5\,\text{Å}$, to the experimental spectra measured with the dimer and the hexamer signals, respectively ($n_{av} = 1960$, the top two spectra of figure 6, black points). For details of the experiment see caption of figure 6. Dashed: calculated contribution of DAA (d-H) molecules, dot-dashed: DDA (d-O) molecules, and dotted: 4-coordinated surface molecules.

although the computed frequency is lower; the discrepancy is most likely due to inaccuracies of the computational model. At larger sizes, a substantial fraction of the DAA intensity moves to higher frequencies (figure 25), and the feature at $\sim 3220\,\mathrm{cm}^{-1}$ originates from DAA molecules (with some contribution from 4-coordinated surface molecules). This feature is visible especially clearly in the dimer spectrum. The infrared absorption of 4-coordinated surface molecules peaks at $3400\,\mathrm{cm}^{-1}$. DDA (d-O) molecules dominate the high frequency end of the bonded-OH band, at $3550\,\mathrm{cm}^{-1}$.

5.4. *Discussion of the dependence of fragment intensity on the mean cluster size*

While comparison of experiment and calculations clearly indicates a photofragment formation process initiated by *surface* radiative excitation, the ensuing molecular mechanism of fragment ejection is unknown. As noted above, preference for hexamers with respect to smaller fragments seems to rule out simple evaporation following energy redistribution within the cluster. Thus, the radiative intramolecular excitation energy is somehow channelled into a *local* intermolecular excitation, and finally into bond breaking and translation of a group of molecules away from the surface. It is seen in the right bottom panel of figure 23, that the probability of hexamer ejection per unit surface of a cold particle maximizes at $\langle n\rangle \sim 70$ molecules. This maximum appears in the amorphous cluster range (see Section 2). As $\langle n\rangle$ increases towards $\langle n\rangle \sim 300$, which corresponds to the onset of a crystal core, photoejection probability drops to very small values.

We then consider the possible fragment ejection mechanism. *Weakly bonded* surface molecules are expected to be removed preferentially. The likely candidates for photoejection are undercoordinated molecules which in fact are present in the surfaces of the model amorphous clusters. In the model structures, however, the calculated *surface density* of the undercoordinated molecules varies by only $\approx 13\%$ with size. Better candidates are therefore *connected groups* of undercoordinated molecules of 4–9 members. Here the percentage is 43% for $n = 48$ and 33% for $n = 123$, and it drops to $\sim 10\%$ in the case of $n = 293$, 600. This result may be related to the enhanced efficiency of hexamer ejection at $\langle n\rangle \sim 70$. Unfortunately, we do not have models for $n = 70$; conceivably, there could be a maximum in the surface density of such groups at this size. The increase of the number of connected undercoordinated molecules with increasing cluster size is apparently a consequence of the larger formation probability, while the decrease is connected to the upcoming number of 4-coordinated molecules. In fact, the ratio $R(3/4)$ of 3- to 4-coordinated molecules is 1.1 for $n = 48$ and drops to $R(3/4) = 0.78$ for $n = 123$, and finally to $R(3/4) = 0.48$ for $n = 293$. However, we still do not know why the fragment size distribution maximizes at the hexamer for cold clusters, and why in warm clusters the fluxes of dimers and hexamers become comparable. One may note that *pairs* of connected 3-coordinated molecules are also common in the cluster surfaces; for $n = 48, 123$, percent participation in pairs is comparable to that in the larger groups; while for $n = 293, 600$ percent participation in pairs is larger.

The decreasing photoejection probability with size, beyond the maximum, is also supported by a different mechanism. The photoejection process, occurs, most likely, in competition with energy redistribution over the cluster. As the amorphous cluster size increases, an increasing fraction of molecules resides in the amorphous core (see figures 8 and 24). Growth of the core is associated with increasing density of core vibrational states, which do not couple significantly to the photoejection channel.

Energy dissipation to these states is expected to become increasingly effective as $\langle n \rangle$ increases. In a particle with a crystal core, competition from energy redistribution should become even more significant. This is since upon crystallization of amorphous ice, the thermal conductivity λ and thus the heat diffusivity D increase by more than a factor of ten [207].

In the known stable hexamer structures, there are 6–9 hydrogen bonds [55, 87–89, 96]. Even if a photofragment adopts one of the stable hexamer structures, its binding energy is most likely lower than that of the sum of the binding energies of the constituent molecules within the particle surface. Some of the energy deficiency could be made up, conceivably, by recombination between remaining molecules within the particle surface; the rest is compensated by the photons. Energy balance considerations lead to the conclusion that at least two photons of $\sim 3500\,\mathrm{cm}^{-1}$ (~ 10 kcal/mol) are necessary to achieve this goal. For the process itself one can imagine a chain (or a ring) of connected 3-coordinated molecules 'unzipping' from the surface, while the remaining dangling atoms of surface molecules are recombining with each other. Perhaps the maximum probability at $\langle n \rangle \sim 70$ corresponds to that surface curvature which makes such recombination effective.

It is thus an interesting unanswered question, what kind of concerted process channels the intramolecular OH-excitation into fragment ejection. In any case this process is particularly efficient following excitation of the *free* OH, as evidenced by the large intensity of the free-OH feature in the experimental spectra (figures 6 and 25). The relative intensity of this feature in the computed absorption spectra of the surface is much lower. As noted in Section 4.3, for small cluster sizes the calculation may underestimate the free-OH intensity. However the bonded-OH/free-OH intensity ratio, calibrated against FTIR spectra of 4 nm particles, is likely to be approximately valid for $\langle n \rangle = 1960$ (5 nm; see figure 10). Thus the relatively low computed infrared *absorption* intensity of the free-OH is likely to be correct. Therefore, the high intensity of this feature in the photofragment spectra should be due to compensation by enhanced probability of energy transfer from OH-excitation to the photoejection coordinate. Since the free-OH frequency is not resonant with the particle interior OH spectrum, reduced competition from energy redistribution to the particle core should favour photoejection. But such reduced competition would not help in absence of an efficient mechanism to channel the free-OH excitation to the hydrogen bond breaking. Evident presence of such a mechanism is quite surprising, considering that the H-atom of the excited bond does *not* participate itself in hydrogen bonding.

6. Summary and concluding remarks

Large water clusters were explored using a number of experimental and computational tools. The OH-stretch spectroscopy was used as the main experimental probe of hydrogen bonding, and as a bridge between computations and experiment. From these investigations, a fairly consistent picture emerges of low energy water cluster structures in the size range of tens–thousands of molecules. In the size range of tens – low hundreds of H_2O, the cluster structures are proposed to be compact-amorphous, such as the ones shown in figure 1. At $n \sim 300$ molecules, a strained crystal core emerges in the cluster interior. At $n \geq 1000$ (diameter ≥ 4 nm), cluster structures can be described as quasi-spherical, with a crystal interior and a disordered reconstructed surface of thickness ~ 5 Å (figure 2). The reconstruction

can be viewed as resulting from recombination of surface dangling atoms, to increase the number of hydrogen bonds, and to reduce the number of undercoordinated molecules. The surface layer includes five- and four-membered water rings, in addition to six-membered ones, while the six-membered rings dominate the crystal interior. Below the disordered surface, a $\sim$5 Å thick subsurface layer consists of mostly crystalline ice with H-bonds strained by interaction with the disordered component. The outer surface, of the extent $\sim$1.5 Å is dominated by 3-coordinated molecules with dangling-H and dangling-O.

We now summarize the computational and experimental tools used in the investigations presented in this review, and the specific results obtained with these tools.

The calculations, described in Section 2, focused on a search for low energy structures of select $(H_2O)_n$ sizes, $n = 48$, 123, 293, 600 and 931. The clusters in this size range are characterized by a huge number of possible structures, so the exploration of the configuration space was, by necessity, far from complete. Still, the compact amorphous structures for $n = 48$, 123 were demonstrated, in our view, reasonably convincingly. Such structures were obtained both from optimization of initially amorphous structures, and from optimization of structures cut from a crystal. A selection of 'special' ordered structures for $n = 48$ (a sandwich, and tubes of four- and six-membered rings) corresponded to significantly higher energies than the optimized amorphous minima. There is probably a large number of additional amorphous minima of similar (and perhaps lower) energies than the ones found by us. Still, the qualitative features of the latter appear consistent with the experimental evidence. The amorphous clusters are characterized by a comparable abundance of the five- and six-membered rings throughout the cluster volume, and a significant contribution from the four-membered ones as well (figure 8).

For the larger cluster sizes ($n = 293$, 600, 931), the lowest energy structures were obtained by optimizing spherical shapes cut from the known nanocrystal structure (ice Ic [5–10]); the optimization resulted in surface reconstruction as described above. For example, for $n = 931$, the number of dangling-O/dangling-H atoms was reduced by multiplying factors 0.57/0.44 in the course of the optimization, with respect to the unrelaxed crystal sphere.[4] Initially amorphous structures yielded significantly higher final energies at these sizes. A preliminary investigation (not described above) was also carried out on whether one can lower the $n = 931$ energy by enclosing the nanoparticle by *crystal* surfaces, at the expense of the deviation from sphericity; the answer seems to be negative.

Calculations of OH stretch spectra of the optimized structures employed the exciton model. The OH bonds were treated as local Morse oscillators coupled by intramolecular and intermolecular dipole–dipole coupling. The model employs an empirical calibration relating the bond frequency to the electric field at the OH-bond (and thus to the hydrogen bond strength). The OH-stretch spectrum was evaluated quantum-mechanically at the minimum energy configuration of the cluster.

[4] In the unrelaxed $(H_2O)_{931}$ sphere cut from ice Ic crystal there are 168/194 d-O/d-H atoms. Recombination during direct minimization reduces the dangling atoms' numbers to 128/126. Further reduction to 96/86 is obtained in the lowest energy optimized cluster structure.

The semi-quantitative level of agreement with experiment appears sufficient for the interpretation of the experimental spectra in terms of the structural elements of the clusters; see figures 3–7.

Section 3 addressed FTIR spectroscopy of particles containing 200 to 10^6 molecules, measured in a cluster cell. Methods were developed for sizing particles from spectroscopic data, by estimation of the volume to surface area ratios. The surface area was estimated by covering the nanoparticles by a monolayer of CF_4, and measuring the intensity of the adsorbate asymmetric stretch band. Advantage was taken of the unique spectroscopic signature corresponding to the monolayer coverage (maximal LO-TO splitting). The volume was estimated using the bonded-OH absorption intensity. Additional estimate of the cluster surface area was based on the integrated intensity of the dangling-OH band, however there is evidence for changes in the d-H surface density with size, at $n \leq 1000$.

Based on these sizing methods, it was possible to measure the evolution of the cluster spectra with $\langle n \rangle$ (figure 4). For $\langle n \rangle \geq 1000$, the spectra could be decomposed to three distinct contributions, assigned to surface, subsurface, and crystal interior (figure 14). The interior component peaks at $3220\,\mathrm{cm}^{-1}$; the subsurface spectrum peaks at a similar frequency but is broader. The very broad surface spectrum, peaking at $3260\,\mathrm{cm}^{-1}$ and extending as far as $3600\,\mathrm{cm}^{-1}$ was assigned to the reconstructed disordered surface layer (see figure 2, bottom panel). The peak of the surface spectrum is dominated by 4-coordinated molecules with a distorted coordination shell; while the undercoordinated molecules contribute at both ends of this spectrum. At cluster sizes of several hundred molecules, the 'well-crystallized' spectroscopic contribution disappears; however the spectra can be still decomposed to the *same* surface and subsurface contributions. The reduced crystal core, stretched by the interactions with the disordered surface, now yields the subsurface signature. Finally, at $n \sim 200$, clusters are too small to support a crystal core, and the spectra indicate amorphous structure.

Studies of interactions with adsorbates are an interesting additional source of information on water clusters. For example, a cold nanocrystal surface ($T \sim 50\,\mathrm{K}$) was shown to be a poor solvent with respect to HCl and HBr acids, a result which was interpreted in terms of paucity of dangling H- and O-atoms in the reconstructed particle surface [177, 178]. At higher temperatures, exposure to a variety of intermediate and strong adsorbates was shown to increase both the dangling-OH intensity, and the intensity of the crystal contribution to the nanoparticle spectrum. This finding was attributed to partial de-reconstruction of the particle surfaces by the adsorbates, initiated by the cleavage of the strained surface hydrogen bonds. The de-reconstruction results in additional favourable binding sites for the adsorbate, while at the same time releasing some strain within the particle; thus improving the interior H-bond network. Studies of the response to SO_2 adsorbate enabled separation of the surface and subsurface contributions to the nanocrystal spectra.

In Section 4, the measurements of the FTIR spectra were extended across the amorphous range, down to the size of several tens of molecules. The measurements were carried out with the help of a new cluster cell system introduced by Baurecker *et al.* (figure 17), which enabled measurements at temperatures as low as 4.5 K. Small $\langle n \rangle$ values could be accessed since the critical nucleus size decreases with temperature. Interpretation of the spectra was complicated by the presence of N_2 impurity attached to the d-H atoms, which increases the free-OH band intensity by a size-dependent factor. The size estimation was carried out based on the blueshift

of the bonded-OH peak with decreasing size, and the comparison of the measured and the computed band shapes.

As the size decreases from $n \sim 400$ to $n \sim 100$ and the clusters become wholly amorphous, the bonded-OH peak frequency shifts from 3267 to $\sim 3310\,\mathrm{cm}^{-1}$ (figure 5). At sizes of a few tens of molecules, about half of H_2O are 3-coordinated; and the contribution of the undercoordinated molecules to the bonded-OH band becomes comparable to that of the 4-coordinated ones. A feature due to the 'companion' bonded-OH of the d-H molecules appears in the low frequency end of the spectrum at $3213\,\mathrm{cm}^{-1}$. At the high frequency end, a $3512\,\mathrm{cm}^{-1}$ feature was assigned to N_2-coated d-O molecules. The peak of the 4-coordinated absorption is blueshifted to $3414\,\mathrm{cm}^{-1}$, due to the increasing H-bond strain with the decreasing cluster size.

Section 5 describes photofragment spectroscopy of water clusters in molecular beams. This technique is shown to be an interesting probe of the *outer* cluster surface, of 1.5 Å thickness, dominated by undercoordinated molecules. The clusters are generated in adiabatic expansions into the vacuum and their size distribution is determined by doping with single Na atoms which are, in turn, detected by photoionization close to the threshold [26]. The mean size range investigated covered $\langle n \rangle = 20$–1960. Vibrational spectroscopy of the OH-stretch mode was carried out by detecting photodesorption of cluster fragments from the parent cluster surface. Among the photodesorption products, there is a strikingly large abundance of water hexamers, and (to a lesser extent) pentamers and tetramers. With cold parent clusters, the hexamers are easily detected, while dimers are undetectable; in a warm beam the respective signals are similar. This is in contrast to the fragment distribution expected for simple heating of the cluster with subsequent evaporation; there, a monomer is expected to be the main product, with a rapid fall-off as a function of size. Thus, the photodesorption mechanism appears to correspond to some kind of complex collective event, in which OH excitation at the cluster surface is channelled to intermolecular motion of a group of H_2O, away from the rest of the cluster.

While the molecular level mechanism of this interesting process is unknown, there is good qualitative agreement between the measured vibrational predissociation spectrum (given by the intensity of the fragments), and the computed infrared absorption spectrum of the outer cluster surface of ~ 1.5 Å depth (figure 6). Thus the molecules which are able to convert the absorbed IR-photon into the intermolecular motion are mainly 3-coordinated and located near the surface. The bonded-OH band of the photofragment spectrum is dominated by 3-coordinated DDA (d-O) molecules at $3500\,\mathrm{cm}^{-1}$, and by DAA (d-H) molecules at $\leq 3220\,\mathrm{cm}^{-1}$. The contribution of the outermost 4-coordinated molecules with a strongly distorted coordination shell peaks at $3400\,\mathrm{cm}^{-1}$. The broad photofragment spectrum displays modest variation with size, as compared to that of the FTIR absorption spectra (figures 4 and 5). Even at small sizes with a large percentage of surface molecules there is a remarkable difference between the photofragment and FTIR spectra (figure 26). The photofragment spectra are also significantly different from the nanocrystal surface spectrum deduced from the analysis of FTIR spectra in a cold condensation cell as presented in Section 3; this is since the method employed in that study associated a significantly thicker layer of molecules of about 5 Å with the surface.

The efficiency of photodesorption is very sensitive to the parent cluster size. The intensity of fragments rises from $\langle n \rangle = 25$ to a peak at about $\langle n \rangle = 70$, and falls off to

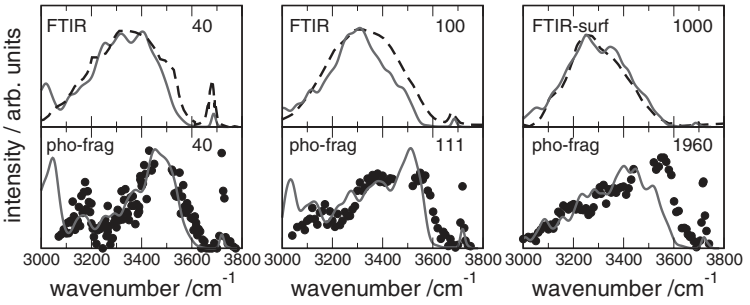

Figure 26. Comparison of the OH-stretch spectra for the mean sizes indicated, obtained from FTIR (dashed lines, see figures 5 and 14) and photofragment spectroscopy (points; see figure 6 and bottom panel of figure 25). FTIR-surf denotes surface contribution to the $\langle n \rangle = 1000$ spectrum, as estimated in Section 3. The solid lines are calculations for $n = 48$, 123 and 931. Bottom panels: calculated spectra for the 1.5 Å thick outer surface layer. Top panels: calculated absorption spectra of the entire clusters $n = 48$ and 123; calculated spectrum for the 5 Å thick surface layer of $n = 931$.

about $\langle n \rangle = 300$ where a long tail begins. Apparently, the photofragment method is mainly sensitive to amorphous structures. The high efficiency of photoejection per unit surface at $\langle n \rangle \sim 70$ may be due to presence of *connected* groups of under-coordinated molecules in the surface. The decrease in the photoejection efficiency for $\langle n \rangle > 70$ is likely to be related to the decrease in the abundance of such groups, and also to the increasingly effective competition from energy redistribution throughout the cluster. Excitation of the free-OH band is associated with particularly efficient photoejection, as evidenced by the high intensity of the free-OH feature in the photofragment spectra (figure 6).

While considerable extent of consistency was reached by combining the different computational and experimental tools, there is still much to be done towards complete understanding of the water clusters. The effect of cluster size distribution on the size estimation methods described in Section 3 should be explored. One should also examine the possibility of agglomeration of suspended ice nanoparticles in cluster cells into loosely bound superstructures [153]. Spectra in the size range of tens of H_2O are needed, without the N_2 impurity which could conceivably modify the structure. On the other hand, the possibility of reshaping of water clusters by adsorbates is worthy of detailed investigation in itself. Molecular mechanisms, by which the OH stretch excitation leads to the hexamer photodesorption from $(H_2O)_n$ clusters in the molecular beam experiments, is an exciting unsolved mystery.

The database of the computed cluster structures should be expanded, and the structure and size distribution effects on the computed spectra should be explored. Also, a number of developments would improve the calculations of the absorption spectra. One is inclusion of the bending overtone; exploratory calculations suggest a noticeable modification of the OH spectra in the vicinity of 3400 cm^{-1}. The coupling between the inter- and intramolecular motions should also eventually be taken into account, e.g., to assess the temperature effect on the spectra [117, 208]. In a more realistic representation, the OH-bond frequency should not reflect the H-bonding at the minimum, but rather, the H-bonding averaged over the intermolecular motions. This effect was already included in studies of small water clusters ($n = 6$–10), and found significant [25, 105–107]. In the present study, the underestimation of the d-H 'companion' frequency in the small cluster spectra is likely to be due to the neglect

of such averaging effect (figures 3, 5, 6). Another theoretical problem is lack of detailed information on the dependence of the bond dipole derivative on the H_2O bonding environment; this information is needed for accurate modelling of spectroscopic contributions from undercoordinated molecules.

Acknowledgements

Israel Science Foundation and the National Science Foundation of the USA are acknowledged for funding. The work in Göttingen was supported by the Deutsche Forschungsgemeinschaft in SFB 357 and in Graduiertenkolleg 782.

References

[1] Vaida, V., Tuck, A. F., Goss, L. M., Daniel, J. S., and Kjaergaard, H., 1999, ACS Abstracts, ACS Meeting at New Orleans, **218**, 403-Phys., Part 2 August 1999.
[2] Molina, M. J., Tso, T. L., Molina, L. T., and Wang, F. C. Y., 1987, *Science*, **238**, 1253.
[3] McCoustra, M. Rs. S., and Horn, A. B., 1994, *Chem. Soc. Rev.*, **23**, 195.
[4] Tielens, A. G. G. M., and Allamandola, L. J., 1987, in *Physical Processes in Interstellar Clouds*, edited by G. E. Morfill and M. Scholet (Dordrecht: Reidel).
[5] Torchet, G., Schwartz, P., de Feraudy, M. F., and Raoult, B., 1983, *J. chem. Phys.*, **79**, 6196.
[6] Torchet, G., Farges, J., de Feraudy, M. F., and Raoult, B., 1989, *Ann. Phys. Fr.*, **14**, 245.
[7] Huang, J., and Bartell, L. S., 1994, *J. phys. Chem.*, **98**, 7455.
[8] Huang, J., and Bartell, L. S., 1995, *J. phys. Chem.*, **99**, 3924.
[9] Huang, J., and Bartell, L. S., 1995, *J. phys. Chem.*, **100**, 8197.
[10] Bartell, L. S., and Chushak, Y. G., 2003, in *Water in Confining Geometries*, edited by V. Buch and J. P. Devlin (Berlin: Springer), Chapter 16.
[11] Hobbs, P. V., 1974, *Ice Physics* (Oxford: Clarendon).
[12] Petrenko, V. F., and Whitworth, R. W., 1999, *Physics of Ice* (New York: Oxford University Press).
[13] Buch, V., Sandler, P., and Sadlej, J., 1998, *J. phys. Chem.* B, **102**, 8641.
[14] McDonald, S., Ojamäe, L., and Singer, S. J., 1998, *J. phys. Chem.* A, **102**, 2824.
[15] Kuo, J. L., Ciobanu, C. V., Ojamäe, L., Shavitt, I., and Singer, S. J., 2003, *J. chem. Phys.*, **118**, 3583.
[16] Torchet, G., de Feraudy, M. F., Boutin, A., and Fuchs, A. H., 1996, *J. chem. Phys.*, **105**, 3671.
[17] Maillet, J. B., Boutin, A., and Fuchs, A. H., 1999, *J. chem. Phys.*, **111**, 2095.
[18] Buch, V., Delzeit, L., Blackledge, C., and Devlin, J. P., 1996, *J. phys. Chem.*, **100**, 3732.
[19] Van de Waal, B. W., Torchet, G., and de Feraudy, M. F., 2000, *Chem. Phys. Lett.*, **331**, 57.
[20] Kroes, G. J., 1992, *Surf. Sci.*, **275**, 365.
[21] Devlin, J. P., Joyce, C., and Buch, V., 2000, *J. phys. Chem. A*, **104**, 1974.
[22] Devlin, J. P., Buch, V., 2003, in *Water in Confining Geometries*, edited by V. Buch and J. P. Devlin (Berlin: Springer), Chapter 17.
[23] Kazimirski, J. K., and Buch, V., 2003, *J. phys. Chem. A*, **103**, 4933.
[24] Buck, U., and Steinbach, C., 2003, in *Water in Confining Geometries*, edited by V. Buch and J. P. Devlin (Berlin: Springer), Chapter 3.
[25] Steinbach, C., Andersson, P., Kazimirski, J. K., Buck, U., Buch, V., and Beu, T. A., 2004, *J. phys. Chem. A*, **108**, 6165.
[26] Bobbert, C., Schütte, S., Steinbach, C., and Buck, U., 2002, *Eur. Phys. J. D*, **19**, 183.
[27] Buch, V., and Devlin, J. P., 1999, *J. chem. Phys.*, **110**, 3437.
[28] Whalley, E., 1977, *Can. J. Chem.*, **55**, 3429.
[29] Fraser, G. T., 1991, *Internat. Rev. Phys. Chem.*, **10**, 189.
[30] Scheiner, S., 1994, *Ann. Rev. phys. Chem.*, **45**, 23.

[31] Chalasinski, G., Szczesniak, M. M., Cieplak, P., and Scheiner, S., 1991, *J. chem. Phys.*, **94**, 2873.
[32] Gonzalez, L., Mo, O., Yanez, M., and Elguero, J., 1996, *J. Mol. Struct. (Theochem)*, **371**, 1.
[33] Knochenmuss, R., and Leutwyler, S., 1992, *J. chem. Phys.*, **96**, 5233.
[34] Van Duijneveldt-van de Rijdt, J. G. C. M., and van Duijneveldt, F. B., 1993, *Chem. Phys.*, **175**, 271.
[35] Van Duijneveldt-van de Rijdt, J. G. C. M., and van Duijneveldt, F. B., 1995, *Chem. Phys. Lett.*, **237**, 560.
[36] Kim, J., Majumdar, D., Lee, H. M., and Kim, K. S., 1999, *J. chem. Phys.*, **110**, 9128.
[37] Kim, J., Majumdar, D., Lee, H. M., and Kim, K. S., 1994, *Chem. Phys. Lett.*, **219**, 243.
[38] Kim, K., Jordan, K. D., and Zwier, T. S., 1994, *J. Amer. Chem. Soc.*, **116**, 11568.
[39] Jensen, J. O., Krishnan, P. N., and Burke, L. A., 1995, *Chem. Phys. Lett.*, **241**, 253.
[40] Jensen, J. O., Krishnan, P. N., and Burke, L. A., 1995, *Chem. Phys. Lett.*, **246**, 13.
[41] Jensen, J. O., Krishnan, P. N., and Burke, L. A., 1996, *Chem. Phys. Lett.*, **260**, 499.
[42] Xantheas, S. S., 1994, *J. chem. Phys.*, **100**, 7523.
[43] Xantheas, S. S., 1995, *J. chem. Phys.*, **102**, 4505.
[44] Fowler, J. E., and Schaefer, H. F., 1995, *J. Amer. Chem. Soc.*, **117**, 446.
[45] Kahn, A., 1995, *J. phys. Chem.*, **99**, 12450.
[46] Estrin, D. A., Paglieri, L., Corongiu, G., and Clementi, E., 1996, *J. phys. Chem.*, **100**, 8701.
[47] Khan, A., 1996, *Chem. Phys. Lett.*, **258**, 574.
[48] Kryachko, E. S., 1997, *Chem. Phys. Lett.*, **272**, 132.
[49] Pedulla, J. M., and Jordan, K. D., 1998, *Chem. Phys. Lett.*, **291**, 78.
[50] Guiang, C. S., and Wyatt, R. E., 1998, *Internat. J. Quantum Chem.*, **68**, 233.
[51] Jiang, J. C., Chang, J. C., Wang, B. C., Lin, S. H., Lee, Y. T., and Chang, H. C., 1998, *Chem. Phys. Lett.*, **289**, 373.
[52] Chaban, G. M., Jung, J. O., and Gerber, R. B., 1999, *J. chem. Phys.*, **111**, 1823.
[53] Wales, D. J., 1999, *J. chem. Phys.*, **111**, 8429.
[54] Day, P. N., Pachter, R., Gordon, M. S., and Merrill, G. N., 2000, *J. chem. Phys.*, **112**, 2063.
[55] Losada, M., and Leutwyler, S., 2002, *J. chem. Phys.*, **117**, 2003.
[56] Bai, J., Su, C. R., Parra, R. D., Zeng, X. C., Tanaka, H., Koga, K., and Li, J. M., 2003, *J. chem. Phys.*, **118**, 3913.
[57] Anick, D. J., 2003, *J. phys. Chem. A*, **107**, 1348.
[58] Chihaia, V., Adams, S., and Kuhs, W. F., 2004, *Chem. Phys.*, **297**, 271.
[59] Stillinger, F. H., and David, C. W., 1980, *J. chem. Phys.*, **73**, 3384.
[60] Weber, T. A., and Stillinger, F. H., 1988, *J. phys. Chem.*, **87**, 4277.
[61] Plummer, P. L. M., and Chen, T. S., 1983, *J. phys. Chem.*, **87**, 4190.
[62] Reimers, J. R., and Watts, R. O., 1984, *Chem. Phys.*, **85**, 83.
[63] Pillardy, J., Olszewski, K. A., and Piela, L., 1992, *J. Mol. Struct. (Teochem)*, **270**, 277.
[64] Farantos, S. C., Kapetanikis, S., and Vegiri, A., 1993, *J. phys. Chem.*, **97**, 12158.
[65] Eggen, B. R., Marks, A. J., Murrel, J. N., and Farantos, S. C., 1994, *Chem. Phys. Lett.*, **219**, 247.
[66] Wales, D. J., and Ohmine, I., 1993, *J. chem. Phys.*, **98**, 7245.
[67] Wales, D. J., and Ohmine, I., 1993, *J. chem. Phys.*, **98**, 7257.
[68] Tsoo, C., and Brooks, C. L., 1994, *J. chem. Phys.*, **101**, 6405.
[69] Sremaniak, L. S., Perera, L., and Berkowitz, M. L., 1996, *J. chem. Phys.*, **105**, 3715.
[70] Jung, J. O., and Gerber, R. B., 1996, *J. chem. Phys.*, **105**, 10332.
[71] Fredj, E., Gerber, R. B., and Ratner, M. A., 1996, *J. chem. Phys.*, **105**, 1121.
[72] Niesse, J. A., and Mayne, H. R., 1997, *J. Comp. Chem.*, **18**, 1233.
[73] Pedulla, J. M., and Jordan, K. D., 1998, *Chem. Phys.*, **239**, 593.
[74] Pedulla, J. M., and Jordan, K. D., 1998, *Chem. Phys. Lett.*, **291**, 78.
[75] Wales, D. J., and Hodges, M. P., 1998, *Chem. Phys. Lett.*, **286**, 286.
[76] Li, Z., Laidig, K. E., and Daggett, V., 1998, *J. Comp. Chem.*, **19**, 60.

[77] Baba, A., Tanaka, J., Saito, S., Matsumoto, M., and Ohmine, I., 1998, *J. Mol. Liquids*, **77**, 95.
[78] Burnham, C. J., Li, J., Xantheas, S. S., and Leslie, M., 1999, *J. chem. Phys.*, **110**, 4566.
[79] Dang, L. X., 1999, *J. chem. Phys.*, **110**, 1527.
[80] Tanaka, H., Yamamoto, R., Koga, K., and Zeng, X. C., 1999, *Chem. Phys. Lett.* **304**, 378.
[81] Qian, J., Stockelman, E., and Hentschke, R., 1999, *J. Mol. Model.*, **5**, 581.
[82] Nigra, P., and Kais, S., 1999, *Chem. Phys. Lett.*, **305**, 433.
[83] Egorov, A. V., Brodskaya, E. N., and Laaksonen, A., 2002, *Mol. Phys.*, **100**, 941.
[84] Guimaraes, F. F., Belchior, J. C., Johnston, R. L., and Roberts, C., 2002, *J. chem. Phys.*, **116**, 8327.
[85] Hartke, B., 2003, *Phys. Chem. Chem. Phys.*, **5**, 275.
[86] Bai, J., Su, C. R., Parra, R. D., Zeng, X. C., Tanaka, H., Koga, K., and Li, J. M., 2003, *J. chem. Phys.*, **118**, 3913.
[87] Kim, K. S., Dupuis, M., Kie, G. C., and Clementi, E., 1986, *Chem. Phys. Lett.*, **131**, 451.
[88] Dykstra, C. E., 1989, *J. chem. Phys.*, **91**, 6472.
[89] Franken, K. A., Jalaie, M., and Dykstra, C. E., 1992, *Chem. Phys. Lett.*, **198**, 59.
[90] Sabo, D., Bacic, Z., Bürgi, T., and Leutwyler, S., 1995, *Chem. Phys. Lett.*, **244**, 283.
[91] Tsai, C. J., and Jordan, K. D., 1991, *J. chem. Phys.*, **95**, 3850.
[92] Tsai, C. J., and Jordan, K. D., 1993, *J. phys. Chem.*, **97**, 5208.
[93] Lee, C., Chen, H., and Fitzgerald, G., 1995, *J. chem. Phys.*, **102**, 1266.
[94] Olthof, E. H. T., van der Avoird, A., and Wormer, P. E. S., 1996, *J. chem. Phys.*, **105**, 8034.
[95] Olthof, E. H. T., van der Avoird, A., Wormer, P. E. S., Liu, K., and Saykally, R. J., 1996, *J. chem. Phys.*, **105**, 8051.
[96] Gregory, J. K., and Clary, D. C., 1996, *J. phys. Chem.*, **100**, 18014.
[97] Hartke, B., Schutz, M., and Werner, H. J., 1998, *Chem. Phys.*, **239**, 561.
[98] Liu, K., Cruzan, J. D., and Saykally, R. J., 1996, *Science*, **271**, 929.
[99] Huisken, F., Kaloudis, M., and Kulcke, A., 1996, *J. chem. Phys.*, **104**, 17.
[100] Liu, K., Brown, M. G., Carter, C., Saykally, R. J., Gregory, J. K., and Clary, D. C., 1996, *Nature*, **381**, 501.
[101] Nauta, K., and Miller, R. E., 2000, *Science*, **287**, 293.
[102] Steinbach, C., Andersson, P., Melzer, M., Kazimirski, J. K., Buck, U., and Buch, V., 2004, *Phys. Chem. Chem. Phys.*, **6**, 3320.
[103] Diken, E. G., Robertson, W. H., and Johnson, M. A., 2004, *J. phys. Chem.* A, **108**, 64.
[104] Buck, U., Ettischer, I., Melzer, M., Buch, V., and Sadlej, J., 1998, *Phys. Rev. Lett.*, **80**, 2578.
[105] Brudermann, J., Melzer, M., Buck, U., Kazimirski, J. K., Sadlej, J., and Buch, V., 1999, *J. chem. Phys.*, **110**, 10649.
[106] Sadlej, J., Buch, V., Kazimirski, J. K., and Buck, U., 1999, *J. phys. Chem.*, **103**, 4933.
[107] Brudermann, J., Buck, U., and Buch, V., 2002, *J. phys. Chem.* A, **106**, 453.
[108] Pribble, R. N., and Zwier, T.S., 1994, *Science*, **265**, 75.
[109] Gruenloh, C. J., Carney, J. R. Hagemeister, F. C., Zwier, T. S., and Jordan, K. D., 2000, *J. chem. Phys.*, **113**, 2290.
[110] Watanabe, T., Ebata, T., Tanabe, S., and Mikami, N., 1996, *J. chem. Phys.*, **105**, 408.
[111] Schmitt, M., Jacoby, C., Roth, W., and Kleinermanns, K., 1998, *J. phys. Chem.* A, **102**, 4471.
[112] Gruenloh, C. J., Carney, J. R., Arrington, C. A., Zwier, T. S., Fredericks, S. Y., and Jordan, K. D., 1997, *Science*, **276**, 1678.
[113] Roth, W., Schmitt, M., Jacoby, C., Spangenberg, D., Janzen, C., and Kleinermanns, K., 1998, *Chem. Phys.*, **239**, 1.

[114] Jorgensen, W. L., Chandrasekhar, J., Madura, J. D., Impey, R. W., and Klein, M. L., 1983, *J. chem. Phys.*, **79**, 926.
[115] Burnham, C. J., and Xantheas, S. S., 2002, *J. chem. Phys.*, **116**, 5115.
[116] Chaplin, M. F., 2000, *Biophys. Chem.*, 83, 211; http://www.lsbu.ac.uk/water/clusters.html.
[117] Clapp, M. L., Miller, R. E., and Worsnop, D. R., 1995, *J. phys. Chem.*, **99**, 6317.
[118] Paul, J. B., Provencal, R. A., Chapo, C., Roth, K., Casaes, R., and Saykally, R. J., 1999, *J. chem. Phys. A*, **103**, 2972.
[119] Goss, L. M., Sharpe, S. W., Blake, T. A., Vaida, V., Brault, J. W., 1999, *J. phys. Chem. A*, **103**, 8620.
[120] Delzeit, L., private communication.
[121] Delzeit, L., and Blake, D., 2001, *J. Geophys. Res. – Planets*, **106**, (E12), 33371.
[122] Weimann, M., Farnik, M., and Suhm, M. A., 2002, *Phys. Chem. Chem. Phys.*, **4**, 3933.
[123] Bauerecker, S., Taraschewski, M., Weitkamp, C., and Cammenga, H. K., 2001, *Rev. Sci. Instrum.*, **72**, 3946.
[124] Buch, V., and Devlin, J. P., 1991, *J. chem. Phys.*, **94**, 4091.
[125] Devlin, J. P., Sadlej, J., and Buch, V., 2001, *J. phys. Chem.* A, **105**, 974.
[126] Kuo, J. L., Coe, J. V., Singer, S. J., Band, Y. B., and Ojamäe, L., 2001, *J. chem. Phys.*, **114**, 2527.
[127] Wawak, R. J., Wimmer, M. M., and Scheraga, H. A., 1992, *J. phys. Chem.*, **96**, 5138.
[128] Kazimirski, J., 2004, PhD Thesis, Hebrew University.
[129] Berry, R. S., 1990, *J. Chem. Soc. Farad. Trans.*, **86**, 2343.
[130] Berry, R. S., 1999, *Theory of Atomic and Molecular Clusters*, edited by J. Jellinek (Berlin: Springer).
[131] Barkema, G. T., and de Boer, J., 1993, *J. chem. Phys.*, **99**, 2059.
[132] Buch, V., 1992, *J. chem. Phys.*, **97**, 726.
[133] Anderson, A. B., 1975, *J. chem. Phys.*, **63**, 1499.
[134] Anderson, A. B., 1976, *J. chem. Phys.*, **65**, 4121.
[135] Li, Z., and Scheraga, H. A., 1987, *Proc. Natl. Acad. Sci. USA*, **84**, 6611.
[136] Burnham, C. J., and Xantheas, S. S., 2002, *J. chem. Phys.*, **116**, 1500.
[137] Wales, D. J., Doye, J. P. K., Miller, M. A., Mortenson, P. N., and Walsh, T. R., 2000, *Adv. chem. Phys.*, **115**, 1.
[138] Matsumoto, M., Saito, S., and Ohmine, I., 2002, *Nature*, **416**, 409.
[139] Xia, X. F., Perera, L., Essmann, U., and Berkowitz, M. L., 1995, *Surf. Sci.*, **335**, 401.
[140] Xia, X. F., and Berkowitz, M. L., 1995, *Phys. Rev. Lett.*, **74**, 3193.
[141] Svishchev, I. M., and Kusalik, P. G., 1994, *Phys. Rev. Lett.*, **73**, 975.
[142] Svishchev, I. M., and Kusalik, P. G., 1996, *J. Amer. Chem. Soc.*, **118**, 649.
[143] Wojcik, M., Buch, V., and Devlin, J. P., 1993, *J. chem. Phys.*, **99**, 2332.
[144] Rowland, B., Kadagathur, S., Devlin, J. P., Buch, V., Feldmann, T., and Wojcik, M., 1995, *J. chem. Phys.*, **102**, 8328.
[145] Reimers, J. R., and Watts, R. O., 1983, *Chem. Phys. Lett.*, **94**, 222.
[146] Rice, S. A., Bergren, M. S., Belch, A. C., and Nielson, G., 1983, *J. phys. Chem.*, **87**, 4295.
[147] Johnson, W. G., Buch, V., and Trenary, M., 1990, *J. chem. Phys.*, **93**, 9167.
[148] Wilson, E. B., Decius, J. C., and Cross, P. C., 1980, *Molecular Vibrations* (New York: Dover).
[149] Whalley, E., and Klug, D. D., 1986, *J. chem. Phys.*, **84**, 78.
[150] Ikawa, I., and Maeda, S., 1968, *Spectrochim. Acta A*, **24**, 655.
[151] Hermansson, K., Lingren, J., and Probst, M. M., 1995, *Chem. Phys. Lett.*, **233**, 371.
[152] Hermansson, K., Knuts, S., and Lingren, J., 1991, *J. chem. Phys.*, **95**, 7486.
[153] Friedlander, S. K., 2000, *Smoke, Haze and Dust* (New York: Oxford University Press).
[154] Hernandez, J., Uras, N., and Devlin, J. P., 1998, *J. chem. Phys.*, **108**, 4525.
[155] Devlin, J. P., and Buch, V. B., 1995, *J. Phys. Chem.*, **99**, 16534.

[156] Ewing, G. E., and De Sheng, T., 1988, *J. Phys. Chem.*, **92**, 4062.
[157] Uras, N., and Devlin, J. P., 2000, *J. phys. Chem. A*, **104**, 5770.
[158] Delzeit, L., Devlin, J. P., and Buch, V., 1997, *J. chem. Phys.*, **107**, 3726.
[159] Decius, J. C., and Hexter, R. M., 1977, *Molecular Vibrations in Crystals* (New York: McGraw-Hill).
[160] Califano, S., Schettino, V., and Neto, N., 1981, *Lattice Dynamics of Molecular Crystals* (Berlin: Springer).
[161] Fox, D., and Hexter, R. M., 1964, *J. chem. Phys.*, **41**, 1125.
[162] Jones, L., and Swanson, B. I., 1991, *J. phys. Chem.*, **95**, 2701.
[163] Gertner, B. J., and Hynes, J. T., 1996, *Science*, **271**, 1563.
[164] Clary, D. C., and Wang, L., 1997, *J. Chem. Soc., Faraday Trans.*, **93**, 2763.
[165] Casassa, S., 2000, *Chem. Phys. Lett.*, **321**, 1.
[166] Kang, H., Shin, T. H., Park, S. C., Kim, I. K., and Han, S. J., 2000, *J. Am. Chem. Soc.*, **122**, 9842.
[167] Allouche, A., Couturier-Tamburelli, I., and Chiavassa, T., 2000, *J. phys. Chem. B*, **104**, 1497.
[168] Svanberg, M., Pettersson, J. B. C., and Bolton, K., 2000, *J. phys. Chem.* A, **104**, 5787.
[169] Mantz, Y. A., Geiger, F. M., Molina, L. T., Molina, M. J., and Trout, B. L., 2001, *Chem. Phys. Lett.*, **348**, 285.
[170] Uras, N., Buch, V., and Devlin, J. P., 2000, *J. phys. Chem.* B, **104**, 9203.
[171] Hagen, W., Tielens, A. G. G. M., and Greenberg, J. M., 1981, *Chem. Phys.*, **56**, 367.
[172] Bertie, J. E., Ahmed, M. K., and Eysel, H. H., 1989, *J. phys. Chem.*, **93**, 2210.
[173] Gough, T. E., and Wang, T., 1996, *J. chem. Phys.*, **105**, 4899.
[174] Bonnamy, A., Georges, R., Benidar, A., and Boissoles, J., 2003, *J. chem. Phys.*, **118**, 3612.
[175] Fleyfel, F., Richardson, H. H., and Devlin, J. P., 1990, *J. phys. Chem.*, **94**, 7032.
[176] Kunzmann, M. K., Bauerecker, S., Suhm, M. A., and Signorell, R., 2003, *Spectrochim. Acta* A, **59**, 2855.
[177] Devlin, J. P., Aytemiz-Uras, N., Sadlej, J., and Buch, V., 2002, *Nature*, **417**, 269.
[178] Buch, V., Sadlej, J., Aytemiz-Uras, N., and Devlin, J. P., 2002, *J. phys. Chem.*, **106**, 9374.
[179] Sadlej, J., Rowland, B., Devlin, J. P., and Buch, V., 1995, *J. chem. Phys.*, **103**, 4804.
[180] Kunzmann, M. K., Signorell, R., Taraschewski, M., and Bauerecker, S., 2001, *Phys. Chem. Chem. Phys.*, **3**, 3742.
[181] Dillmann, A., and Meier, G. E. A., 1989, *Chem. Phys. Lett.*, **160**, 71.
[182] Dillmann, A., and Meier, G. E. A., 1991, *J. chem. Phys.*, **94**, 3872.
[183] Becker, R., and Döring, W., 1935, *Ann. Phys.*, **24**, 719.
[184] Viisanen, Y., Strey, R., and Reiss, H., 1993, *J. chem. Phys.*, **99**, 4680.
[185] Bauerecker, S., submitted to *Phys. Rev. Lett.*
[186] Taraschewski, M., Cammenga, H. K., Bauerecker, S., and Tuckermann, R., *J. phys. Chem.*, to be published.
[187] Miller, R., Anderson, R. J., Kassner, J. L., and Hagen, D. E., 1983, *J. chem. Phys.* **78**, 3204.
[188] Marti, J., and Mauersberger, K., 1993, *Geophys. Res. Lett.* **20**, 363.
[189] Hinds, W. C., 1999, *Aerosol Technology* (New York: John Wiley).
[190] Karapetian, K., and Jordan, K. D., 2003, in *Water in Confining Geometries*, edited by V. Buch and J. P. Devlin (Berlin: Springer), Chapter 6.
[191] Albert, S., Bauerecker, S., and Quack, M., 2003, *The Eighteenth Colloquium on High Resolution Molecular Spectroscopy, 8–12* September 2003, Dijon, France.
[192] Buck, U., and Huisken, F., 2000, *Chem. Rev.*, **100**, 3863.
[193] Vernon, M. F., Krajnovich, D. J., Kwok, H. S., Lisy, J. M., Shen, Y. R., and Lee, Y. T., 1982, *J. chem. Phys.*, **77**, 47.
[194] Huisken, F., Mohammad-Pooran, S., and Werhahn, O., 1998, *Chem. Phys.*, **239**, 11.
[195] Buck, U., Gu, X. J., Lauenstein, C., and Rudolph, A., 1990, *J. chem. Phys.*, **92**, 6017.

[196] Buck, U., and Ettischer, I., 1998, *J. chem. Phys.*, **108**, 33.
[197] Huisken, F., Kulcke, A., Voelkel, D., Laush, C., and Lisy, J. M., 1993, *Appl. Phys. Lett.*, **62**, 805.
[198] Hagena, O. F., 1981, *Surf. Sci.*, **106**, 101.
[199] Hagena, O. F., 1987, *Z. Phys.* D, **4**, 291.
[200] Ahmed, M., Apps, C. J., Hughes, C., and Whitehead, J. C., 1994, *J. phys. Chem.*, **98**, 12530.
[201] Vostrikov, A. A., and Dubov, D. Y., 1991, *Z. Phys.* D, **20**, 429.
[202] Buck, U., and Winter, M., 1994, *Z. Phys.* D, **31**, 291.
[203] Ewing, G. E., 1978, *Chem. Phys.*, **29**, 253.
[204] Beswick, J. A., and Jortner, J., 1981, *Adv. Chem. Phys.*, **47**, 363.
[205] Buck, U., 1993, in *Dynamical Processes in Molecular Physics*, edited by G. Delgado-Barrio (Bristol: IOP), p. 275.
[206] Buck, U., 1995, *Adv. At. Mol. Opt. Phys.*, **35**, 121.
[207] Andersson, O., and Suga, H., 1994, *Solid State Comm.*, **91**, 985.
[208] Sivakumar, T. C., Rice, S. A., and Sceats, M. G., 1978, *J. chem. Phys.* **69**, 3468.